

AD-A107 073

NORTHROP RESEARCH AND TECHNOLOGY CENTER PALOS VERDES --ETC F/8 20/5  
DEVICE DEVELOPMENT PROGRAM FOR EFFICIENT EXCITATION OF A BLUE-B--ETC(U)  
MAY 80 D E ROTHE, W H LONG  
N00014-78-C-0831  
NL

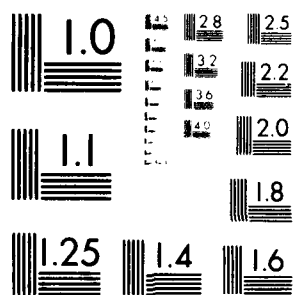
UNCLASSIFIED

11-1  
10-10-14



10-10-14

END  
DATE  
FILED  
10-10-14  
BTIC



MICROCOPY RESOLUTION TEST CHART  
NATIONAL BUREAU OF STANDARDS-1963-A

CONFIDENTIAL 12

# DEVICE DEVELOPMENT PROGRAM for EFFICIENT EXCITATION of a BLUE-GREEN LASER

**D.E. Rothe and W.H. Long, Jr.**  
**NORTHROP CORPORATION**  
**Northrop Research and Technology Center**  
**One Research Park**  
**Palos Verdes Peninsula, California 90274**

DTIC  
ELECTE  
NOV 9 1981

## July 1980

**Final Technical Report  
for Period 21 August 1978 – 20 August 1979  
Contract N00014-78-C-0831**

1941

Approved for public release;  
Distribution Unlimited

**PREPARED FOR:**  
**OFFICE of NAVAL RESEARCH**  
**800 North Quincy Street**  
**Arlington, Virginia 22217**

81 11 06 071

#### ACKNOWLEDGEMENTS

The dedicated efforts and very capable assistance of Messrs. D. Avant, R. Lunden, and H. Stone in constructing and testing of the electric-discharge devices are gratefully acknowledged.

|                    |  |
|--------------------|--|
| Accession For      |  |
| NTIS CPA&I         | <input checked="checked" type="checkbox"/> |
| DTIC TAB           | <input type="checkbox"/>                   |
| Unannounced        | <input type="checkbox"/>                   |
| Justification      |  |
| By                 |  |
| Distribution/      |  |
| Availability Codes |  |
| A                  |  |

UNCLASSIFIED

SECURITY CLASSIFICATION OF THIS PAGE (When Data Entered)

| REPORT DOCUMENTATION PAGE   |                                     | READ INSTRUCTIONS<br>BEFORE COMPLETING FORM  |
|---|-------------------------------------|--|
| 1. REPORT NUMBER<br>NRTC-80-10R   | 2. GOVT ACCESSION NO.<br>AD-A107073 | 3. RECIPIENT'S CATALOG NUMBER  |
| 4. TITLE (and Subtitle)<br>DEVICE DEVELOPMENT PROGRAM FOR EFFICIENT<br>EXCITATION OF A BLUE-GREEN LASER   |                                     | 5. TYPE OF REPORT & PERIOD COVERED<br>Final Technical Report.<br>21 Aug 1978—20 Aug 1979 |
| 7. AUTHOR(s)<br>D. E. Rothe and W. H. Long, Jr.   |                                     | 6. PERFORMING ORG. REPORT NUMBER<br>NRTC 80-10R  |
| 9. PERFORMING ORGANIZATION NAME AND ADDRESS<br>Northrop Research & Technology Center<br>One Research Park<br>Palos Verdes Peninsula, California 90274   |                                     | 8. CONTRACT OR GRANT NUMBER(s)<br>N00014-78-C-0831                                       |
| 11. CONTROLLING OFFICE NAME AND ADDRESS<br>Office of Naval Research<br>800 North Quincy Street<br>Arlington, Virginia 22217   |                                     | 10. PROGRAM ELEMENT PROJECT TASK<br>AREA & WORK UNIT NUMBERS                             |
| 14. MONITORING AGENCY NAME & ADDRESS (if different from Controlling Office)<br>1282   |                                     | 12. REPORT DATE<br>May 1980  |
|   |                                     | 13. NUMBER OF PAGES<br>76  |
|   |                                     | 15. SECURITY CLASS. (of this report)<br>Unclassified                                     |
|   |                                     | 15a. DECLASSIFICATION DOWNGRADING<br>SCHEDULE  |
| 16. DISTRIBUTION STATEMENT (of this Report)   |                                     |  |
| 17. DISTRIBUTION STATEMENT (of the abstract entered in Block 20, if different from Report)  |                                     |  |
| 18. SUPPLEMENTARY NOTES   |                                     |  |
| 19. KEY WORDS (Continue on reverse side if necessary and identify by block number)<br>Self-Sustained Discharge-Excited XeCl Laser, Longitudinal Discharge,<br>Transverse Preionization Pulse, High-Voltage Pulse Networks, Parametric<br>Study and Optimization of XeCl Laser   |                                     |  |
| 20. ABSTRACT (Continue on reverse side if necessary and identify by block number)<br>A novel transverse/longitudinal double-discharge device, operated as an XeCl laser, has been evaluated as part of an effort to increase the efficiency of discharge-excited lasers for the Navy's proposed blue-green communications system. Experimental results showed that the stable operating regime of such a device is limited to gas compositions and pressures which do not optimize the chemical laser kinetics for the rare-gas halides. Theoretical computer predictions are compared with the experimental results. |                                     |  |

DD FORM 1473  
1 JAN 73EDITION OF 1 NOV 65 IS OBSOLETE  
S/N 0102-014-6601

407696

UNCLASSIFIED

SECURITY CLASSIFICATION OF THIS PAGE (When Data Entered)

## CONTENTS

|  | <u>Page</u> |
|--|-------------|
| 1.0 SUMMARY  | 1           |
| 2.0 INTRODUCTION   | 2           |
| 2.1 Navy Blue-Green Laser Requirements                               | 2           |
| 2.2 Alternative Blue-Green Laser Systems                             | 3           |
| 2.3 UV-Pump Laser Configurations                                     | 6           |
| 2.4 Review of Self-Sustained Discharge-<br>Excited RGH Laser Work    | 7           |
| 3.0 APPROACH   | 16          |
| 3.1 Impedance Matching for Transverse<br>and Longitudinal Discharges | 17          |
| 3.2 Description and Principle of Operation<br>of LTDD Device         | 20          |
| 3.3 Design of Marx Bank  | 24          |
| 4.0 EXPERIMENTAL RESULTS   | 30          |
| 4.1 Common-Electrode LTDD Device                                     | 32          |
| 4.1.1 Direct Marx Drive  | 32          |
| 4.1.2 Pulse-Forming Networks   | 35          |
| 4.2 Separate-Electrode LTDD Device                                   | 53          |
| 4.3 Variations in Discharge Geometry                                 | 55          |
| 4.4 Effects of Gas Additives   | 56          |
| 5.0 THEORETICAL ANALYSIS   | 57          |
| 5.1 Circuit and Discharge Modeling                                   | 57          |
| 5.2 Discharge Kinetics   | 65          |
| 6.0 CONCLUSIONS  | 72          |
| 7.0 REFERENCES   | 74          |
| LIST OF FIGURES  | iii         |

# LIST OF FIGURES

| <u>Figure</u> |  | <u>Page</u> |
|---------------|--|-------------|
| 1             | 200 W Blue-Green Raman-Shifted XeCl Electric Discharge Laser (Overall Efficiency = 1%)   | 5           |
| 2             | Schematic of UV-Preionized Transverse Discharge Laser  | 10          |
| 3             | Transverse Discharge Geometry  | 10          |
| 4             | Pictorial View of Spark-Preionized Transverse Discharge Device   | 11          |
| 5             | Discharge Characteristics for 1L Transverse Discharge Laser (KrF)  | 13          |
| 6             | Transverse/Longitudinal Double-Discharge Configuration   | 21          |
| 7             | Series Configuration of Parallel Discharge Circuits  | 24          |
| 8             | Electrical Schematic for High-Voltage Pulse Generator (12 Stage Marx Bank)   | 25          |
| 9             | Parallel Charging Capacitance ( $C_{PAR}$ ) and Series Discharge Capacitance ( $C_{SER}$ ) of Marx Bank for Marx Configurations A and B  | 26          |
| 10            | Electrical Energy ( $E$ ) Stored in Marx Bank as a Function of Charging Voltage ( $V_{CH}$ ) for Marx Configurations A and B   | 28          |
| 11            | Longitudinal-Discharge XeCl Laser.   | 29          |
| 12            | Construction of LTDD Device With Common Electrodes   | 33          |
| 13            | Typical Arc Pattern Observed When Gas Mixture is too Rich in Xenon   | 34          |
| 14            | Current and Laser Pulse for Marx Bank (Conf. A) Feeding LTDD Directly ( $V_{CH} = 40$ kV)  | 36          |
| 15            | Electric Pulse Generator for TLDD Laser  | 37          |
| 16            | Pulse Shapes of Discharge Voltage ( $V_D$ ) and Current ( $I_D$ ), Current in Peaking Circuit ( $I_{PK}$ ), Electric Power Deposited in Discharge ( $P_E$ ), and Optical Power ( $P_O$ ) | 39          |

# LIST OF FIGURES (Contd)

| <u>Figure</u> |   | <u>Page</u> |
|---------------|---|-------------|
| 17            | Current Oscillations in an Underdamped RLC Circuit  | 41          |
| 18            | Current Oscillations in Peaking Circuit ( $C_{PK} = 100$ pF) as a Function of Laser Gas Mixture   | 43          |
| 19            | Electrode Shapes of Surface-Spark Gaps Tested   | 44          |
| 20            | Peaking-Circuit Current (A), Discharge Current (B), and Optical Laser Power (C) with Pulse-Sharpening Rail Gap (39 psi air) and 30 kV Marx Charging Voltage | 47          |
| 21            | Optical Pulse Energy as a Function of Charging Voltage  | 48          |
| 22            | Evolution of Optical Pulse ( $\epsilon_o$ ) from Fluorescence to Lasing with Increasing Electric Energy ( $\epsilon_{EL}$ ) Input                           | 49          |
| 23            | Optical Pulse Energy as a Function of $CCl_4$ Partial Pressure and Xe/ $CCl_4$ ratio for Xe/ $CCl_4$ /He Mixtures at 1300 Torr Total Pressure               | 51          |
| 24            | Optical Pulse Energy as a Function of HCl Partial Pressure and Xe/HCl Ratio for Xe/HCl/He Mixtures at 1300 Torr Total Pressure                              | 52          |
| 25            | Optical Pulse Energy as a Function of Xe Partial Pressure and Xe/HCl Ratio for Xe/HCl/He Mixtures at 1300 Torr Total Pressure                               | 53          |
| 26            | Typical Double-Discharge Circuit with Passive Delay for Separate-Electrode Device   | 55          |
| 27            | One-Stage PFN   | 58          |
| 28            | Waveforms for One-Stage PFN with KrF  | 58          |
| 29            | Two-Stage PFN   | 60          |
| 30            | Waveforms for Two-Stage PFN with KrF  | 60          |
| 31            | Circuit and Discharge Model   | 61          |



LIST OF FIGURES (Contd)

| <u>Figure</u> |   | <u>Page</u> |
|---------------|---|-------------|
| 32(A)         | Results of Model Calculations; $V_o = 300$ kV | 63          |
| 32(B)         | Results of Model Calculations; $V_o = 450$ kV | 64          |
| 33            | Production and Loss of Electrons              | 69          |
| 34            | Rate Constants                                | 70          |
| 35            | Discharge Power Partitioning                  | 71          |

## 1.0 SUMMARY

This experimental and analytical research program was pursued as part of the Navy's laser development effort for a future blue-green satellite-to-submarine communication system. The goal of the program was to improve the efficiency of self-sustained high-pressure discharge lasers emitting in the uv and visible parts of the spectrum. New techniques and discharge geometries, which hold the potential for improving the efficient transfer of electric energy from the capacitors to the discharge, were critically investigated.

A novel double-discharge technique, which incorporates a fast transverse pre-ionization pulse followed by a longitudinal discharge, has been evaluated. Such a geometry provides the possibility of matching the discharge impedance to that of the drive circuit more easily. An extensive parametric study of this device for a wide range of operating conditions and pump pulses showed, however, that reliable, stable discharges and good optical beam quality could only be achieved for gas mixtures which were relatively lean in Xe and in the chlorine donor ( $\text{HCl}$ ,  $\text{BCl}_3$ ,  $\text{CCl}_4$ ); leaner than the mixtures which are optimum<sup>1</sup> for the production of the excited upper laser level of  $\text{XeCl}$ . Highest laser output was 50 mJ of pulse energy at 308 nm with an intrinsic efficiency of 0.5 percent.

Experimentally achieved efficiencies fell short of anticipated performance levels. The major difficulty has been identified as being connected with discharge stability problems, which are known to be very complex for high-pressure gas discharges<sup>2,3</sup> operating in the attachment-limited regime. The longitudinal discharge geometry, combined with the very high voltages (300 kV) and the presence of dielectric surfaces in the vicinity of the discharge, evidently put severe constraints on the stable operating range of such a device. Several discharge chambers with different electrode arrangements and dielectric materials were built and tested with a number of different pulse-forming networks. Similar limitations were observed for all of these configurations.

In parallel with the experiments, a realistic computer model was developed, which predicts the time variance of the discharge impedance. This model is based on theoretical descriptions of the electron, ion and excited-state kinetics in the discharge and on the circuit response to the variable discharge load. Theoretical predictions are compared with actually measured circuit responses for the devices tested.

## 2.0 INTRODUCTION

In connection with the U.S. Navy's technology development program for laser communication with submarines, a reliable 200 - 1000 watt average-power blue-green laser system is required. High overall system efficiency, utmost reliability and long component life are of prime importance for a viable spaceborne laser for this application. There are several alternative approaches for pursuing this goal, although neither can meet the requirements on the basis of its state-of-the-art development.

The existence of efficient frequency down-conversion schemes makes it possible to make full use of the potentially very efficient, rare-gas halide lasers for applications which require high average powers in the blue-green regions of the spectrum. A study,<sup>4</sup> which seeks to maximize the frequency conversion efficiency from the ultraviolet to the blue-green by novel Raman conversion techniques in high-pressure hydrogen, has been pursued at the Northrop Research and Technology Center as a parallel effort and is the subject of a separate report.

An inband laser, which shows considerable promise for eventually meeting the performance specifications, is the mercuric bromide dissociation laser.<sup>5,6</sup> Such a laser has produced<sup>7</sup> over 50 mJ/pulse with one percent efficiency during recent experiments performed at NOSC. No scaling limitations have so far been discovered for this type of laser.

System goals and possible laser candidates for meeting these goals are described in more detail in the following sections.

### 2.1 Navy Blue-Green Laser Requirements

Design goals for the satellite-stationed pulsed blue-green laser for Navy applications are summarized hereunder:

|                             |                        |
|-----------------------------|------------------------|
| Average Power:              | 200 W - 1000 W         |
| Wavelength:                 | 450 nm - 510 nm        |
| Bandwidth:                  | $\leq 0.2 \text{ \AA}$ |
| Pulse Energy:               | 2 J - 10 J             |
| Pulse Repetition Frequency: | 100 Hz - 300 Hz        |

|                     |                                    |
|---------------------|------------------------------------|
| Pulsewidth:         | 50 ns - 500 ns                     |
| Overall Efficiency: | > 1%                               |
| Reliability:        | Space qualifiable for<br>2-5 years |
| Component Life:     | $10^{10}$ pulses                   |

These goals cannot be met by any single laser system available at this time. Concentrated research and development programs are required to advance the state-of-the-art of short wavelength lasers to the stage where such a system can be designed with reasonable confidence.

## 2.2 Alternative Blue-Green Laser Systems

At present the most promising candidates for meeting the systems specifications are the Raman-shifted XeCl laser and the inband HgBr laser, but so far neither approach has met the combined requirements of energy output and laser efficiency. Whereas the basic technologies for efficient electric discharge excitation are identical for XeCl and HgBr, a considerably larger research and development effort has been expended over the past few years on the optimization of rare-gas halide lasers, including XeCl. As a result, there are now several high-PRF lasers available commercially (Lambda-Physik, Lumonics). These have several watts of average-power output with laser efficiencies close to one percent at 308 nm. Scalability of the discharge-excited XeCl laser has also been demonstrated <sup>2,8</sup> to the multijoule level, but an improvement of more than a factor of two is needed in the laser efficiency to meet Navy goals.

XeCl is deemed more suitable than XeF for the pump laser because of the better performance<sup>9</sup> of discharge-pumped XeCl lasers at high pulse frequencies. Also less chemical cleanup<sup>9,10</sup> is required with XeCl, making long-term sealed-off operation possible. The ultraviolet output (308 nm) from the XeCl laser can be shifted into the blue-green (460-490 nm) by highly efficient multi-Stokes vibrational Raman conversion techniques<sup>11</sup> in molecular gases (H<sub>2</sub>, D<sub>2</sub>, HD, CH<sub>4</sub>) or by Raman down-conversion of metallic vapors<sup>12,13</sup> (Ba, Tl, Bi, Pb).

In both Raman media respectable conversion efficiencies have been obtained with the XeCl laser. More recently<sup>4,11</sup> improvements in the Raman conversion efficiency have been achieved with an oscillator-amplifier scheme. These experiments have shown photon efficiencies approaching the quantum limit in the case of higher Stokes-order generation in hydrogen gas. The oscillator-amplifier scheme has also demonstrated the feasibility of generating near-diffraction-limited Stokes radiation. For efficient conversion of the XeCl laser into the blue-green region, atomic lead vapor and molecular hydrogen and deuterium gases appear to be the leading candidates based on the currently available experimental data.

The results of a systems study for a 200 W blue-green laser with one percent overall efficiency are shown in Figure 1. This design is based on 50 percent energy conversion from 308 nm to 472 nm, using one vibrational Raman shift in D<sub>2</sub>, followed by two more Stokes orders in H<sub>2</sub>. An overall systems efficiency of one percent can be realized, if the single-pulse electrical efficiency (without gas compressor and other auxiliary equipment) of the XeCl discharge device is approximately three percent.

Frequency conversion by liquid dyes is no longer considered a practical alternative to Raman processes for the spaceborne system because of the following drawbacks:

1. Dyes have a limited life due to chemical degradation upon exposure to the intense uv laser light.
2. The photon conversion efficiencies for dyes are near 50 percent as compared with 80 percent for Raman processes.
3. Due to heating problems dyes are subject to limitation in average power that can be handled efficiently.

Whereas the rare-gas halide lasers have been studied extensively in the U.S. and abroad, work on the discharge-excited HgBr<sub>2</sub> dissociation laser has until very recently, only been pursued by U.S. Navy laboratories, notably NOSC<sup>5,7</sup> and NRL.<sup>6</sup> Nevertheless, approximately 50 mJ of blue-green laser energy have been extracted with 0.95 percent laser efficiency<sup>7</sup> from an HgBr laser. However, the chemical kinetics for this type of laser are not yet fully understood,

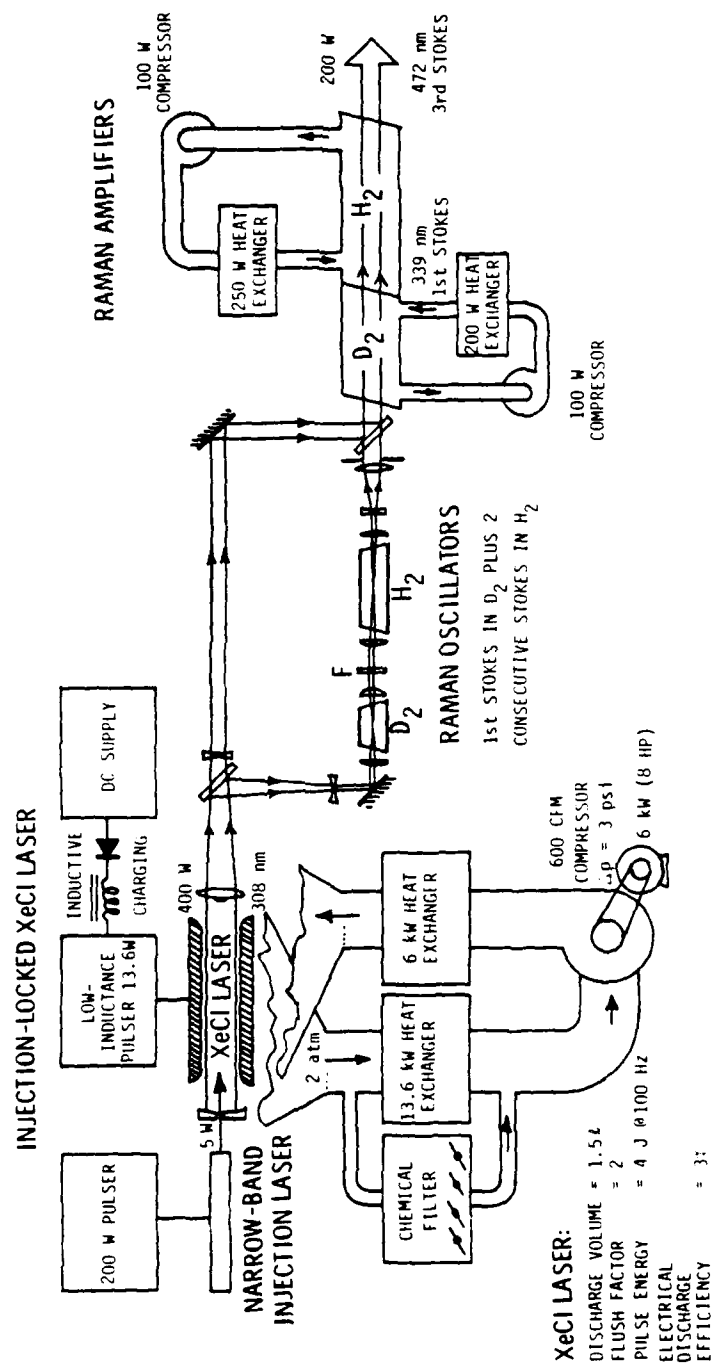


**FIGURE 1. 200 W BLUE-GREEN RAMAN-SHIFTED XeCl ELECTRIC DISCHARGE LASER (OVERALL EFFICIENCY = 1%)**

and the entire operating regime (pressure, gas mixture, temperature, electric power loading,  $E/N$ ) has not been fully investigated. Therefore, considerable potential exists for improving the efficiency further. Furthermore, enough empirical data has been collected on the discharge characteristics in  $\text{HgBr}_2$  laser mixtures, so that scalability to the multijoule levels can safely be predicted for these lasers. Since the  $\text{HgBr}$  laser emits already in the blue-green part of the spectrum, no frequency conversion losses are present to degrade the overall system efficiency. The presently attainable  $\text{HgBr}$  laser efficiency has to be increased by only a factor of 1.35 in order to meet the overall system efficiency goal of one percent.

The work undertaken within the present project, seeking to improve the efficiency of electric discharge excitation of laser gases, is relevant to both the rare-gas halide laser and the mercuric bromide laser.

### 2.3 UV-Pump Laser Configurations

The various configurations of the rare-gas halide (RGH) laser for the Raman-converted  $\text{XeCl}$  system may be categorized in terms of the mode of excitation employed; i.e.

1. Electron-beam pumped laser (opposed e-beams or coaxial gun diode for uniformity of energy deposition and efficient optical extraction).
2. E-beam sustained discharge-excited  $\text{XeCl}$  laser (only advantageous if a large enhancement ratio of discharge power to e-beam power can be realized).
3. Self-sustained discharge-excited laser (for excitation of high-pressure gases the transverse TE-laser geometry has generally been shown to be advantageous).

Higher intrinsic efficiencies have been demonstrated with e-beam devices than with self-sustained discharges, because the gas mixtures, pressures and electron energies can be independently chosen to optimize the laser kinetic processes. With self-sustained discharge devices, efficient operation of the

laser is limited to gas mixtures and E/N values for which a stable glow discharge can be maintained.

The Achilles heel of all e-beam machines, however, is the e-beam window foil, necessary for separating the vacuum diode from the high-pressure laser plenum. Window foils have a finite life due to occasional intense localized heating (cathode plasma striking foil, arcs in laser discharge), metal fatigue (shock waves, repeated heat distortion) and chemical attack (corrosive laser gases). Rupture of the window foil leads to catastrophic failure of the laser system and requires time-consuming repair.

Whereas an e-beam device may be the logical choice for a large ground-based laser (as envisioned by DARPA), its relatively low reliability makes it unattractive for use in a remote high-prf spaceborne system. Increasing the overall efficiency of self-sustained discharge lasers is therefore of vital importance for future Navy missions.

Glow discharges in high-pressure gases are by nature unstable and tend to contract into intense arc channels unsuitable for laser excitation. In pulsed discharges, however, the glow can be maintained for a short duration lasting from a few nanoseconds to several hundred ns, provided the gas is uniformly preionized. Uniform preionization may be provided by:

1. UV-photoionization with spark sources located outside of the discharge volume.
2. Preionization by corona discharge in close proximity of the main discharge.
3. Preionization by a fast uniform (1-10 ns) predischARGE (double-discharge technique).

The device tested in the present work employed a combination of corona and predischARGE for conditioning the gas.

#### 2.4 Review of Self-Sustained Discharge-Excited RGH Laser Work

Self-sustained pulsed discharge devices have several important advantages over e-beam machines. These are:



1. Compactness, simplicity, and high reliability, a prerequisite for air and spaceborne systems.
2. High-prf capability, for high average output powers.
3. High optical beam quality (low refractive index of helium diluent makes the laser beam less sensitive to acoustic disturbances).

As discussed in Section 2.2, the overall efficiency requirements for the 200 W Blue-green Raman-shifted XeCl laser can be met, if the single-pulse electrical efficiency (without flow system and other auxiliary equipment) of the XeCl discharge device is three percent. So far, however, no uv-preionized or double-discharge excited rare-gas halide laser has operated with efficiencies higher than 1.5 percent.

Recent work performed at NRTC (to be described in this section), both experimental and analytical, indicates that there are two basic reasons for the observed low efficiencies in transverse electric discharges:

1. The range of  $E/N$  values, over which the discharge can be operated, is dictated by discharge stability. At the beginning of the discharge pulse, when good power coupling between the circuit and the discharge is taking place, the  $E/N$  value is too high for optimum power conversion to form rare-gas metastables. Near the end of the pulse, when the  $E/N$  value is more favorable, very little power is coupled into the discharge from the circuit, because of severe impedance mismatching.
2. The glow phase in transverse-discharge-excited rare-gas halogen mixtures is unstable. Cathode streamers form shortly after the onset of the current pulse, resulting in fast deterioration of the discharge impedance. The latter generally drops to well below one ohm in a period of a few tens of nanoseconds. A fixed-impedance drive circuit can, therefore, transfer power into the discharge efficiently for only a short transient phase during the discharge development.

The new transverse/longitudinal discharge geometry (tested here) was expected to alleviate both problem areas.

Over the last three years, the Laser Technology Laboratory of the Northrop Research and Technology Center has developed and tested two different uv-preionized TE-lasers, which are described in more detail in the following sections. The data obtained with these lasers makes it possible to pinpoint the basic difficulties and limitations of transverse discharge devices, and hence the limitations imposed on the scaling of such lasers.

A parametric study of a uv-preionized 0.3-liter volume discharge laser was completed during 1977. The device was tested for operation with KrF and XeF, using a variety of fluorine donors and a wide range of gas mixture ratios, gas pressure and discharge voltages. Maximum pulse energies from KrF and XeF at 249 nm and 350 nm were 300 mJ and 180 mJ, respectively, and wall plug efficiency for KrF was one percent. Data relating to laser performance as a function of fluorine donor, gas composition, total pressure, electrode voltage and energy loading were reported in the open literature<sup>14</sup> and were presented at technical conferences.<sup>15,16</sup>

Based on the experience gained from the 0.3 liter device, a larger discharge chamber (one liter) was designed, built, and tested. This laser was built entirely from fluorine-compatible materials, such as aluminum, stainless steel, copper and teflon. A schematic diagram of the discharge and preionization circuit for this laser is shown in Figure 2. A two-stage LC-inversion network was employed to produce the high-voltage discharge pulse. The electrodes in this laser were 50 cm long and were spaced 5 cm apart. The discharge volume was preionized by means of two rows of uv sparks located behind a 50 percent transparent anode, made from perforated stainless steel (Figure 3). The sparks were energized by the LC-inversion current of the pulse-forming network only 50 ns ahead of the discharge pulse. Circuit inductance was kept low by employing 14 closely coupled LC-inversion networks in parallel. The circuits were discharged by means of a specially designed low-inductance 8-channel triggered spark gap, pressurized with a 15 percent SF<sub>6</sub> - 85 percent Ar mixture. All capacitors were conventional oil-filled aluminum-foil capacitors suitable for higher pulse repetition frequencies. They were pulse-charged through a charging inductor and diode just prior to triggering the multichannel spark gap.

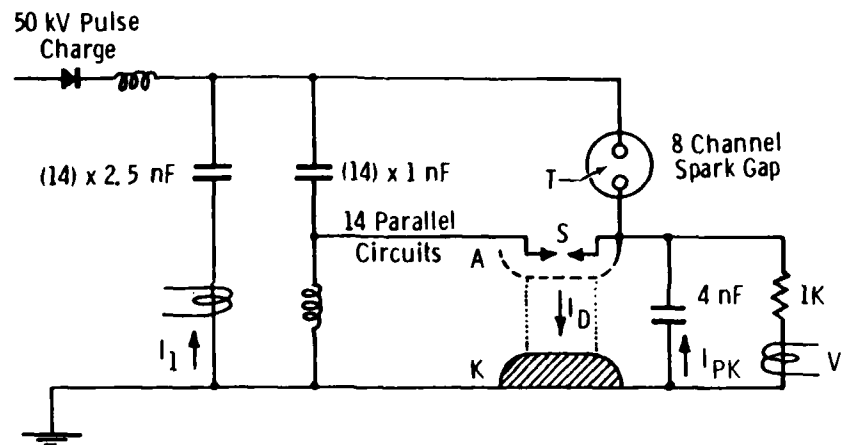


FIGURE 2. SCHEMATIC OF UV-PREIONIZED TRANSVERSE DISCHARGE LASER

80-26

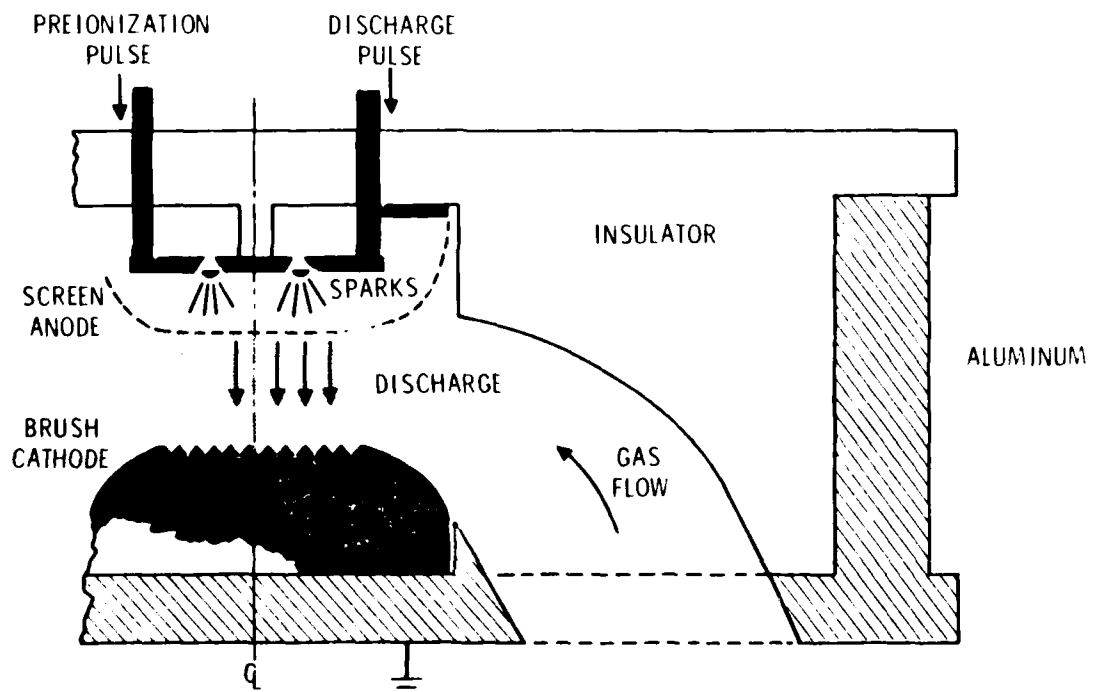


FIGURE 3. TRANSVERSE DISCHARGE GEOMETRY

80-27



FIGURE 4. PICTORIAL VIEW OF SPARK-PREIONIZED  
TRANSVERSE DISCHARGE DEVICE

A pictorial view of this versatile laser test bed is given in Figure 4. The discharge chamber was built to withstand up to 10 atm of gas pressure and provisions were made for future addition of transverse gas flow equipment. Note the close-packed arrangement of discharge capacitors and the multi-channel spark gap on top of the discharge chamber. The coil, visible near the top of the picture, is the charging inductor.

This laser has been operated primarily with KrF and XeCl with output energies in the 0.5 J range. A variety of halogen donors have been employed. Gas mixture ratios, pressures, voltage and current pulses were varied over a wide range. Typical E/N values were  $3 \times 10^{-16}$  V-cm<sup>2</sup> (8 kV/cm-atm), and the energy loading was approximately 80 J/l-atm. Best gas mixtures for KrF (249 nm) and XeCl (308 nm) consisted for F<sub>2</sub>/Kr/He = 3/50/2000 Torr and HCl/Xe/He = 4/20/2000 Torr, respectively. Optical pulse duration was 35 ns, typically, and the overall efficiency was 0.5 percent.

Detailed analysis of the voltage and current input pulses and of the optical output pulse as a function of time have shown that the single most important factor affecting the laser performance is the efficiency with which electrical power is transferred from the circuit to the discharge. Because of impedance mismatch between circuit and rapidly varying load, most of the stored energy is dissipated elsewhere in the circuit or is added to the gas at a rate well below lasing threshold. This condition causes the overall laser efficiency to be less than one percent; even though the intrinsic efficiency, based on electric energy actually added to the gas during the laser pulse, is much larger.

The important portions of the measured voltage and current pulses are reproduced in Figure 5. For these tests a set of barium titanate peaking capacitors (totaling 4 nF) was placed inside the discharge chamber to steepen the current rate-of-rise at the leading edge of the discharge pulse. Charging voltage was 55 kV. Note that the peak voltage (measured externally) reaches only 46 kV, which is less than half the theoretical LC-doubled peak voltage. Evidently, the discharge initiates well before the inversion cycle is complete. The time of discharge initiation is well marked by the sudden drop in voltage and the

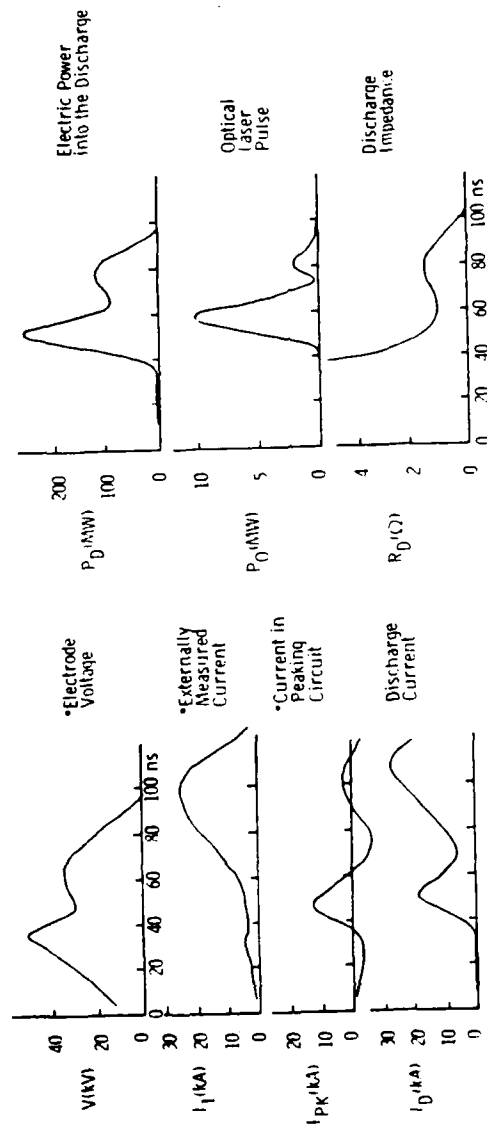


FIGURE 5. DISCHARGE CHARACTERISTICS FOR 1V TRANSVERSE DISCHARGE LASER (KrF)  
(\*Quantities measured directly;  $I_D$ ,  $P_D$  and  $R_D$  curves were derived from the measured parameters.)

simultaneous increase in current. The voltage drops to zero as the current reaches its maximum value. The current going through the discharge ( $I_D$ ) can be derived by adding the peaking circuit current ( $I_{PK}$ ) and the current  $I_1$ , fed into the system by the external circuit. The power ( $P_D$ ) deposited in the gas is then found by multiplying the voltage pulse ( $V$ ) with the discharge current ( $I_D$ ). Note that the power dissipated ( $P_D$ ) displays a pulse shape similar to that of the laser pulse. The first peak is almost entirely due to the energy temporarily stored in the peaking capacitors. The second peak is due to additional energy pumped in by the external capacitors and barely reaches lasing threshold, so that the extracted optical pulse is relatively weak. The discharge impedance ( $R_D$ ), obtained by dividing the  $V$  curve by the  $I_D$  characteristic, exhibits somewhat of a plateau at the one ohm level for approximately 30 ns.

Consider now the amounts of electric energy stored in the various parts of the circuit or dissipated in the discharge for calculating laser efficiencies:

#### Stored or Deposited Amounts of Energy

- |  |       |
|--|-------|
| (a) Total electric energy stored in discharge circuit at 55 kV:  | 74J   |
| (b) Electric energy deposited in discharge as determined from measured $V$ , $I$ -characteristics (integral of $P_D$ curve in Figure 5): | 18.4J |
| (c) Electric energy temporarily stored in low-inductance peaking circuit at 46 kV:   | 4.2J  |

#### KrF Laser Efficiencies

- |  |      |
|--|------|
| (a) Efficiency based on total energy stored in capacitors (wall-plug efficiency):        | 0.5% |
| (b) Efficiency based on total energy deposited in gas, as measured by $V$ , $I$ -probes: | 2.2% |
| (c) Efficiency of first laser spike based on energy stored in peaking capacitors:        | 7%   |

The last figure shows that the intrinsic efficiencies of self-sustained discharge-excited rare-gas halide lasers are not too different from those of e-beam pumped systems. Apparently, the prime reason for the low overall efficiency ( $\approx 1\%$ ) of self-sustained devices lies in their inability to transfer all of the stored energy to the gas at a rate which is consistent with good energy extraction. A discharge pumped KrF or XeCl laser with a 3 percent overall efficiency can evidently be developed, provided that the impedance-matching problem can be solved.



### 3.0 APPROACH

Electric discharge excitation is a simple and convenient method of energizing a gaseous laser medium. Glow discharges in superatmospheric high-power gas lasers (such as the rare-gas halide lasers) are basically unstable, however, and can only be initiated by providing a uniform predischARGE field and a uniform preionization level in the gas. Once established, a distributed glow can then only be maintained for short periods (generally for only a fraction of a microsecond), particularly in gas mixtures containing electro-negative species ( $F_2$ ,  $O_2$ ,  $NF_3$ ,  $SF_6$ ,  $HCl$ , etc.). The glow phase is terminated by the development of cathode streamers, which later coalesce into one or more bright arcs. During the transition phase, streamers and glow may co-exist, and effective laser excitation may still take place, provided the streamers do not extend over the entire cathode-anode gap, and the discharge impedance has not collapsed to a very low value ( $\ll 1 \Omega$ ) as a result.

Electric power transfer from the discharge capacitors to the glow discharge is most efficient if the glow resistance (load impedance) is approximately equal to the characteristic circuit impedance ( $2\sqrt{L/C}$ ). The circuit is critically damped under these conditions, and no current oscillations occur. When the discharge impedance becomes very small due to arc or streamer formations, the discharge circuit becomes highly underdamped, and the electric energy oscillates rapidly between the circuit inductance and the circuit capacitance (period =  $2\pi\sqrt{LC}$ ) with practically no power dissipation in the laser gas.

In the operation of uv-preionized high-pressure transverse-discharge-excited rare-gas halide lasers, cathode streamers form quickly after the onset of the current pulse, resulting in a fast deterioration of the discharge impedance. The latter generally<sup>17</sup> decreases to well below 1 ohm in a period of a few tens of nanoseconds, whereas the applied voltage and current pulses are typically 50 to 100 ns long (determined primarily by circuit inductance). Efficient excitation of the gain medium occurs, therefore, only during a short transient phase of the discharge. This is believed to be the principal reason for the relatively low efficiency (around 1 percent) observed

with self-sustained rare-gas halide lasers using a conventional TE-laser geometry.<sup>14,17-21</sup> Best efficiencies have been achieved with lasers having fast discharge networks<sup>14,17,21,22</sup> with low inductance. Low impedance circuits have been chosen deliberately in an attempt to provide a reasonable match to the extremely low discharge impedance.

The impedance-matching problem (pumping inefficiency) is accentuated by the usual TE-laser geometry. Because of the large cross sectional discharge area and the short discharge length, the resistance of the positive column ( $R = \rho_l/A$ ) is a few ohms at best. Furthermore, the impedance mismatch generally becomes worse when such TE-lasers are scaled up,<sup>16</sup> unless careful consideration is given to this aspect of the problem.

It is, therefore, appropriate to consider alternate discharge geometries for which the anode-cathode spacing is increased and the cross sectional area of the discharge reduced. Specifically, a longitudinal discharge geometry may be expected to provide a much larger discharge impedance, making the design of an impedance-matched circuit easier.

### 3.1 Impedance Matching for Transverse and Longitudinal Discharges

For a series RLC circuit critical damping occurs when  $R = 2\sqrt{L/C}$ . Voltage and current oscillations are thus avoided when

$$L \leq \frac{1}{4} R^2 C. \quad (3.1)$$

If the discharge is the only dissipative element in the circuit, then all the energy stored in the capacitors will eventually end up in the gas. The total energy added per unit discharge volume is then

$$U = \frac{CV^2}{2\phi} \quad (3.2)$$

where

$$\phi = d^2 \ell \quad (3.3)$$

is the discharge volume,  $\ell$  is the length of the gain region and  $d$  is the height and width of the discharge (square optical gain cross section assumed).

Eliminating C between expressions (3.1) and (3.2) gives

$$L \leq \frac{R^2 U \phi}{2 V^2} \quad (3.4)$$

The circuit inductance has to be less than this value for the absence of oscillations.

Consider a transverse discharge first. For that geometry

$$R_T = \rho d/d\lambda = \rho \phi^{-\frac{1}{3}} \alpha^{-\frac{2}{3}} \quad (3.5)$$

and

$$V_T = E d = E \phi^{\frac{1}{3}} \alpha^{-\frac{2}{3}} \quad (3.6)$$

Here  $\rho$  is the resistivity of the positive column of the discharge and  $\alpha = \lambda/d$  is the aspect ratio of the gain volume. For the transverse discharge the inequality (3.4) can therefore be rewritten as

$$L_T \leq \frac{1}{2} \rho^2 E^{-2} U \phi^{-\frac{1}{3}} \alpha^{-\frac{2}{3}} \quad (3.7)$$

For a particular type of discharge-pumped gas laser, the values of  $\rho$ ,  $E$  and  $U$  are fairly well determined by discharge stability criteria and pumping thresholds. Note the negative exponents on  $\phi$  and  $\alpha$ . If either the discharge volume  $\phi$  or the aspect ratio  $\lambda/d$  is increased for a transverse discharge, the circuit inductance has to be reduced to make impedance matching possible. For a longitudinal discharge, however, the situation is reversed. Here

$$R_L = \rho \lambda/d^2 = \rho \phi^{-\frac{1}{3}} \alpha^{\frac{4}{3}} \quad (3.8)$$

and

$$V_L = E \lambda = E \phi^{\frac{1}{3}} \alpha^{\frac{2}{3}} \quad (3.9)$$

so that

$$L_L \leq \frac{1}{2} \rho^2 E^{-2} U \phi^{-\frac{1}{3}} \alpha^{\frac{4}{3}} \quad (3.10)$$

With a longitudinal discharge geometry, the larger the aspect ratio, the larger a circuit inductance can be tolerated.

We can now make a direct comparison between the discharge characteristics of a longitudinal and transverse discharge. With all other variables being

equal ( $\rho, E, U = \text{const.}$ ), it is of interest to see how the pulse lengths, power densities and current densities compare for the two geometries. In the following discussion it will be assumed that the circuit is critically damped.

#### Circuit Impedance

From expressions (3.7) and (3.10) we obtain

$$L_L/L_T = \alpha^2 . \quad (3.11)$$

For example, if the aspect ratio is 10, the inductance of the longitudinal discharge circuit may be 100 times larger than for the transverse geometry.

#### Capacitance

Combination of Equations (3.2), (3.6) and (3.9) gives

$$C_L/C_T = v_T^2/v_L^2 = \alpha^{-2} . \quad (3.12)$$

#### Pulse Length

The full width at half maximum for a critically damped current pulse is

$$\tau_{CR} = 2.45 \sqrt{LC} \quad (3.13)$$

Hence, from relations (3.11) and 3.12) it is evident that

$$\tau_L/\tau_T = 1 . \quad (3.14)$$

In other words, one can work with the same pumping pulse duration in both cases.

#### Power Density

Let the power density be given by

$$P/\phi = U/\tau \phi \quad (3.15)$$

so that

$$(P/\phi)_L/(P/\phi)_T = \tau_T/\tau_L = 1 . \quad (3.16)$$

The longitudinal discharge can thus provide the same pump power density as an equivalent transverse discharge for all aspect ratios.

### Current Density

The current density in the discharge is approximately given by

$$j \approx \frac{CV}{\tau A} = \frac{2U\phi}{V\tau A} \quad (3.17)$$

where A is the cross sectional area of the discharge at right angles to the current flow.

$$\frac{A_L}{A_T} = \frac{d}{L} = \alpha^{-1} . \quad (3.18)$$

Therefore

$$j_L/j_T = (V_T/V_L)(\tau_T/\tau_L)(A_T/A_L) = 1 . \quad (3.19)$$

Since the current densities are the same for the longitudinal and the transverse discharges, the power dissipation per unit volume in the cathode fall regions are also the same (cathode sheath thickness and cathode fall potential are independent of the electrode separation, i.e., the length of the positive column). This means that the temperature rise in the cathode sheath of the longitudinal discharge should be very similar to that occurring in TE-laser discharges. Discharge instabilities originating in the cathode sheath are, therefore, expected to be no worse for the longitudinal discharge geometry than they are for typical TE-lasers.

### 3.2 Description and Principle of Operation of LTDD Device

A unique longitudinal/transverse double discharge (LTDD) laser is described in this section. The gas in this device is preconditioned with a fast uniform transverse discharge and is subsequently pumped by means of a high-impedance longitudinal glow discharge. The original device described here uses a single high-voltage pulse generator to drive both discharges.

The electrode configuration, shown schematically in Figure 6, combines some of the advantages of pulsed transverse excitation with the better load-matching features of the longitudinal discharge. Two long parallel metal electrodes

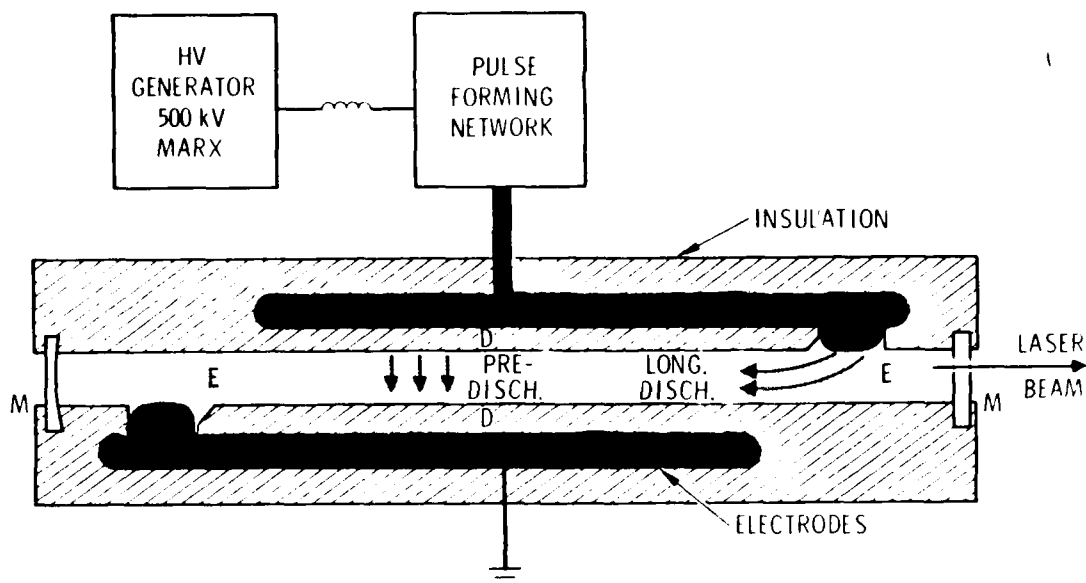


FIGURE 6. TRANSVERSE/LONGITUDINAL DOUBLE-DISCHARGE CONFIGURATION

are arranged as in a TE-laser. These electrodes are totally enclosed in a dielectric material, D, except for an opening, E, at opposite ends, where the electrode metal is in contact with the high-pressure laser gas. The dielectric barrier, D, is of sufficient thickness and dielectric strength to withstand the applied voltage long enough (several nanoseconds) for the longitudinal discharge (from E to E) to become established. The interelectrode space containing the lasing gas is sealed on all sides. The laser oscillator cavity is formed by two reflectors, M, located at the ends of the discharge section. Transverse gas flow can be added easily with this configuration for high pulse repetition rates.

This geometry makes it possible to obtain double discharge excitation of the gas with a single high-voltage pulse obtained from a conventional pulse generator. The discharge sequence will now be described under separate headings of "PredischARGE" and "Main Discharge."

### Predischarge

When the high-voltage pulse first appears on the electrodes, an extremely high transverse field ( $V/p \sim 50\text{-}100 \text{ kV/cm-atm}$ ) is created. Note that initially the field strength through the gas is many times higher than the field in the dielectric,  $D$ , because the dielectric constant for the gas is generally much lower than that for the dielectric insulation. The high field breaks down the gas very rapidly and establishes a uniform glow. Current flows through the gas until the dielectric barrier is fully charged up, and the transverse field in the gas drops to a low value close to zero.

This predischarge pulse is very uniform, since no metallic emitter surfaces are involved. The tendency for discharge contraction, leading to streamer and arc formation is minimized by the fact that the charges on the dielectric surface are immobile. Furthermore, the predischarge pulse length is extremely short and is determined by the circuit inductance,  $L$  (which should be kept reasonably small in any case), and the stray capacitance of the dielectric between the electrodes (a few pF). Even though the energy deposited in the gas during the predischarge pulse is negligibly small, the power density and ionization levels are high. In fact, the gas excitation is high enough, that lasing threshold may be reached during this prepulse; which means that no energy is wasted in the main pump pulse to establish optical gain.

TE-laser preionization by means of a "frustrated" discharge through a dielectric has been employed before,<sup>23,24</sup> but not in conjunction with a longitudinal discharge geometry, not at the voltage levels described here, and not without separate predischarge and delay circuits.

### Main Discharge

The main discharge follows the transverse preconditioning pulse as soon as the gas becomes sufficiently ionized to support the large longitudinal pump current. Since the gas has been very uniformly preionized, it can be expected that the longitudinal discharge will also be very uniform. Transverse charge oscillations may in fact continue during the longitudinal discharge phase. This may further stabilize the main discharge and may permit longer pump pulses and operation at lower, more optimum  $E/N$  values.

Long time delays ( $\Delta t \sim 1 \mu s$ ) between preionization and discharge pulses, generally used with uv-preionized TE-lasers, are not necessary here, because such delays are only required to smooth out an originally nonuniform ionization level by charge recombination. With the present design, the preionization uniformity is excellent to start with. Furthermore, the short time delay ( $\Delta t \sim 2 ns$ ) between predischage and main discharge is a definite asset when electronegative gas species are present. In the presence of halogen compounds, for example, free electrons are rapidly lost by electron attachment to form negative ions, so that the preionization becomes significantly less effective if the discharge does not follow immediately after the preionization pulse.

There are thus many possible advantages in the LTDD design which could lead to a superior discharge laser. The present study was an attempt to develop some of these features into a practical device. The following list summarizes some of the unique considerations of this design:

1. Predischage and main discharge are energized with a single high-voltage pulse.
2. The transverse predischage is a very fast and very uniform glow discharge, containing very little energy. Nevertheless, the power density is very high, resulting in intense excitation and ionization.
3. Lasing threshold may be established during the predischage pulse, so that all the energy in the main discharge becomes available for producing optical gain.
4. The very short delay times between discharge pulses make it possible to effectively preionize electronegative gas mixtures.
5. The longitudinal discharge maintains a large discharge impedance, which can be more easily matched to the circuit impedance over a longer time period for optimum power transfer to the gas.
6. The extremely high voltages required for the longitudinal discharge may be considered a disadvantage in terms of pulse generator complexity and added insulation. This drawback,



however, is offset by the fact that at high voltages a large amount of energy can be stored in a small capacitor (Energy =  $\frac{1}{2} CV^2$ ). Short excitation pulses ( $\tau = 2.4\sqrt{LC}$ ) are, therefore, easily achieved, even when the circuit, inductance,  $L$ , is relatively large.

7. For a low-gain laser medium, it may be desirable to increase the gain length without unduly increasing the discharge length and, thus, the applied voltage. This can easily be accomplished by arranging several discharge sections in series optically, but in parallel electrically (Figure 7).

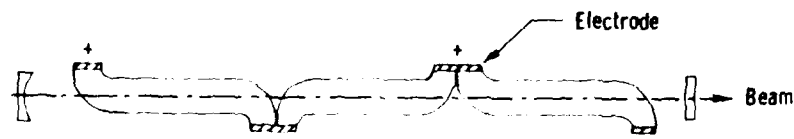


FIGURE 7. SERIES CONFIGURATION OF PARALLEL DISCHARGE CIRCUITS

### 3.3 Design of Marx Bank

In order to generate the very high voltages required for energizing the longitudinal discharge laser, a 12-stage Marx bank was designed and built. A schematic of this unit, which is capable of producing pulses up to 480 kV, is given in Figure 8. During the course of the investigation, two different values for the capacitance per stage were employed, making it possible to apply different pulse energies to the laser network without change in applied voltage (and  $E/N$ ). For configuration A, three 2700 pF "Murata" barium titanate capacitors were paralleled per stage. For the high-energy version (configuration B) five of these capacitors were used per stage. Since the capacitance of these ceramic capacitors is strongly voltage dependent (less capacitance at higher charging voltage), the energy stored in the Marx bank cannot be simply calculated from  $CV^2/2$ , assuming  $C$  constant.

The variation of the Marx charging capacitance (with all capacitors in parallel), as seen by the HV charging supply, is shown in Figure 9 for configurations A and B (left scale). The right-hand scale of Figure 9 gives

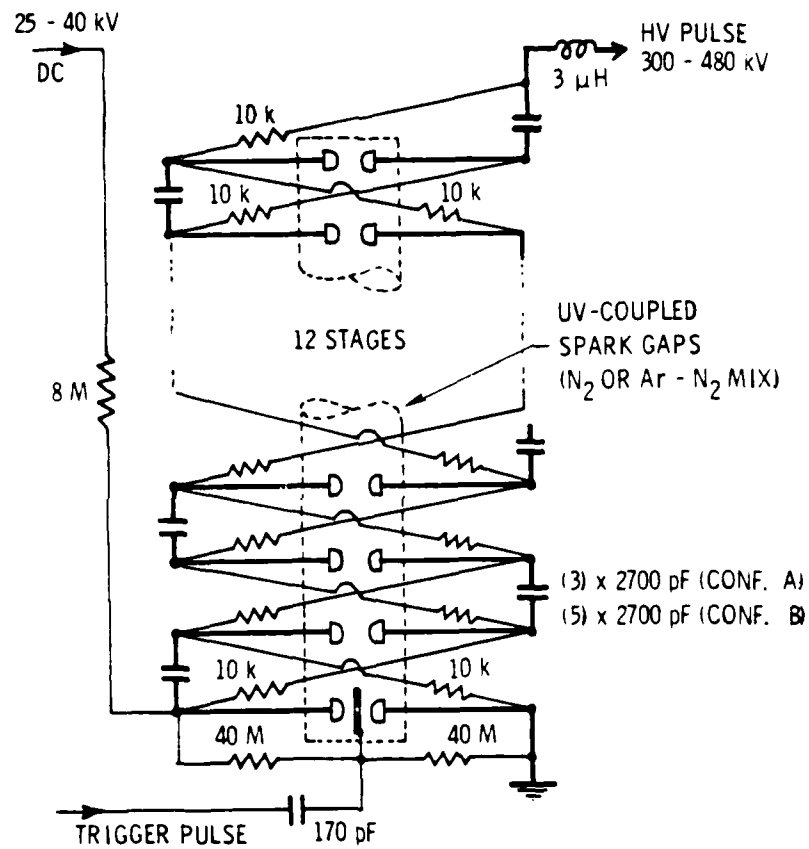


FIGURE 8 . ELECTRICAL SCHEMATIC FOR HIGH-VOLTAGE PULSE GENERATOR (12 STAGE MARX BANK).

30-36

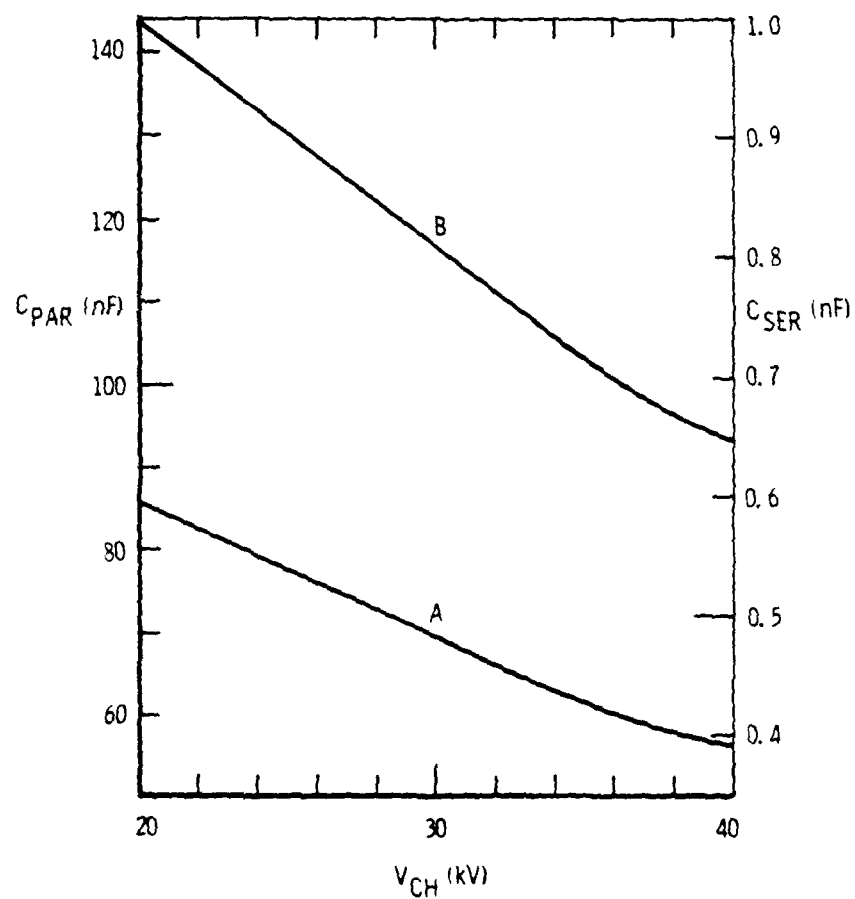


FIGURE 9. PARALLEL CHARGING CAPACITANCE ( $C_{PAR}$ ) AND SERIES DISCHARGE CAPACITANCE ( $C_{SER}$ ) OF MARX BANK FOR MARX CONFIGURATIONS A AND B (NOTE STRONG DEPENDENCE OF CAPACITANCE ON CHARGING VOLTAGE,  $V_{CH}$ ).

the Marx discharge capacitance (with all 12 stages connected in series) as a function of charging voltage. Figure 9 was compiled from data supplied by the capacitor manufacturer. The corresponding electrical energy stored in the Marx bank ( $\mathcal{E}$ ) is shown in Figure 10. At full charging voltage (40 kV/stage) configuration B can store 80 joules. At the same voltage, configuration A contains 45 joules. Note that the voltage dependence of  $\mathcal{E}$  is almost linear with the charging voltage  $V_{CH}$ .

The spark gaps for all 12 stages consisted of 19 mm diameter hemispherical brass electrodes spaced approximately 13 mm apart. All gaps were contained within a single plexiglass tube, which could be pressurized up to 50 psig. During the tests the spark tube was filled with dry nitrogen or with argon-nitrogen mixtures (with lower voltages) at pressures between 5 and 30 psig.

The Marx voltage was erected by triggering the bottom stage with a 50 kV trigger pulse. The trigger pulse was applied to a midplane voltage-grading disc halfway between the first-stage spark electrodes. All other spark gaps were closed by overvoltage and by uv-radiation from the lower-stage spark gaps. In order to achieve a more stable voltage holdoff condition during charging, the electrode spacing was tapered from 12 mm for the first stage to 16 mm for the last stage. All spark gaps, capacitors, charging resistors and voltage dividers were contained in a plexiglass box filled with transformer oil (see Figure 11).

For the duration of the experimental program (approximately 50 000 shots) the Marx bank performed flawlessly without pretriggering or component failure.

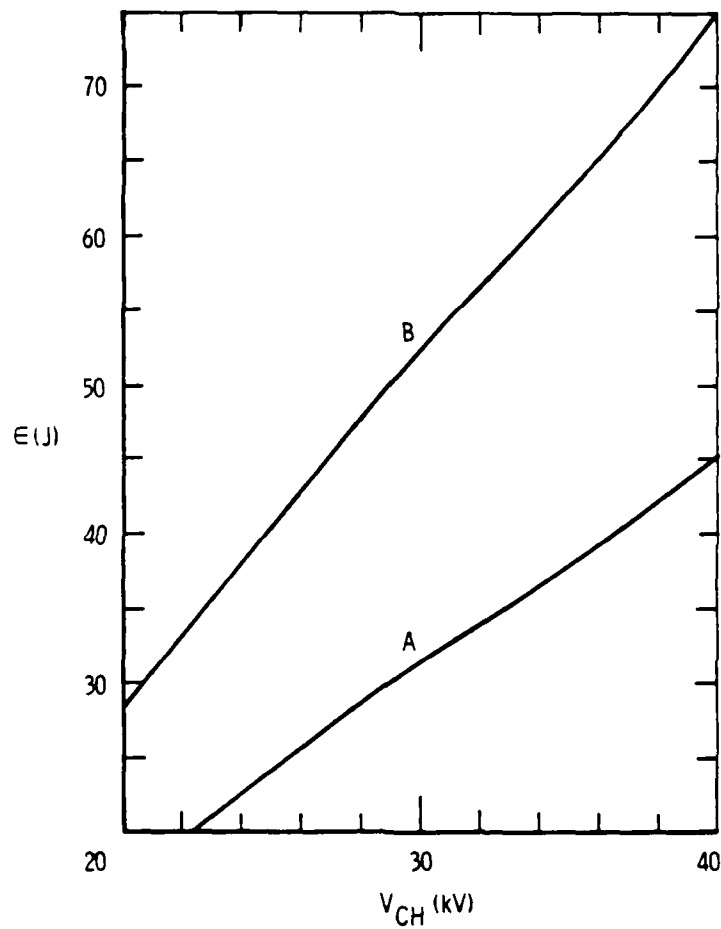


FIGURE 10. ELECTRICAL ENERGY ( $E$ ) STORED IN MARX BANK AS A FUNCTION OF CHARGING VOLTAGE ( $V_{CH}$ ) FOR MARX CONFIGURATIONS A AND B.

30-36

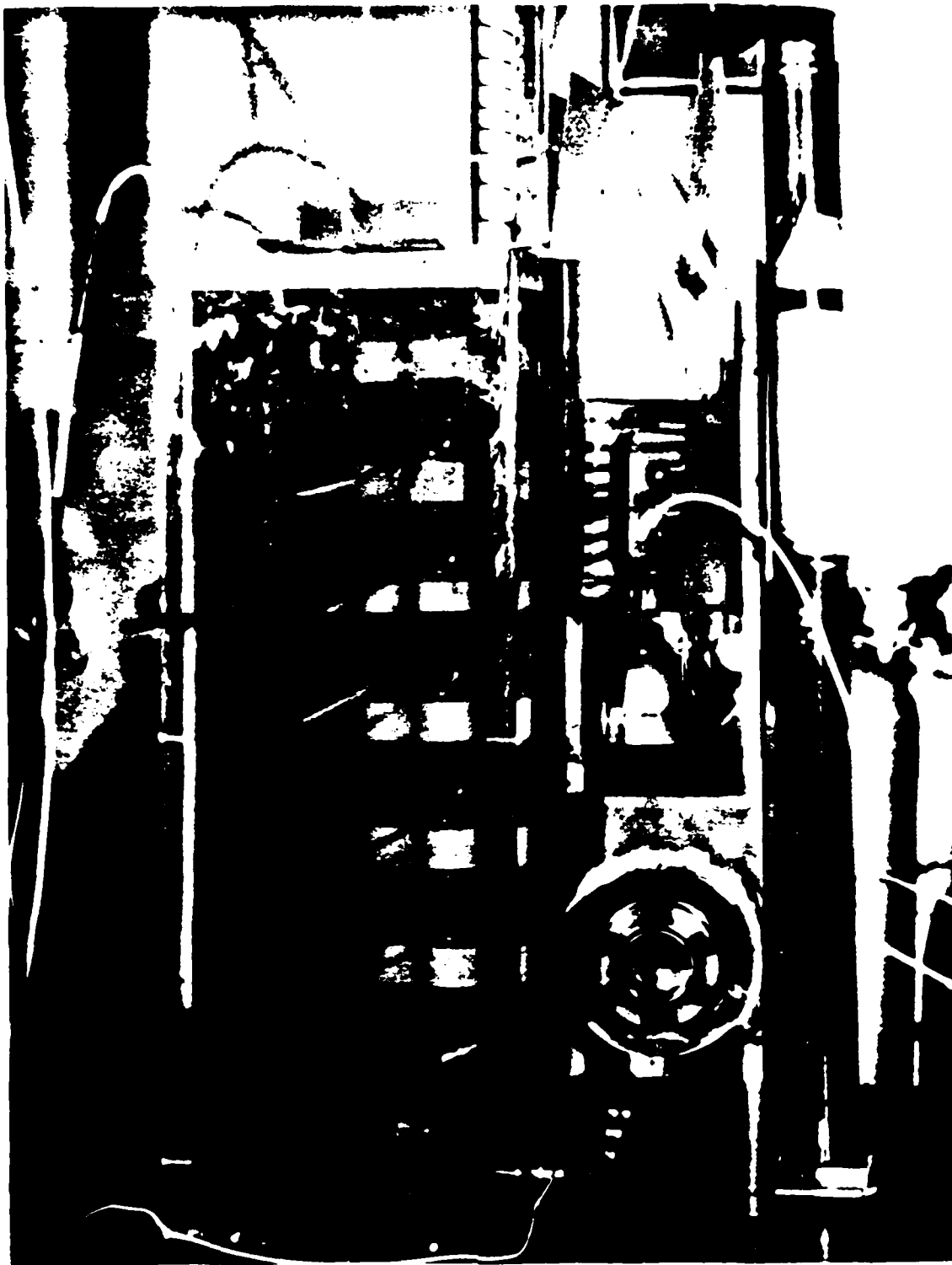


FIGURE 11. LONGITUDINAL-DISCHARGE XeCl LASER. MARX BANK IS AT LEFT, DISCHARGE CHAMBER AND PFN AT RIGHT

#### 4.0 EXPERIMENTAL RESULTS

During the course of the experimental program no fewer than seven LTDD laser cavities were built, using different methods of construction, but adhering to the general geometry described in Section 3.2. Only two of these devices survived even short exposure to the extremely high voltage pulses, which generally exceeded 300 kV. All discharge cavities containing PVC or glass panels failed due to excessive electrical and/or mechanical stresses (see Table 1).

Essentially all experiments described in this report were performed with Devices No. 2 and 7, which were made from alumina-filled casting epoxy and NEMA G-10 boards. In Device No. 2, the transverse and longitudinal discharge electrodes were common, as described in Figure 6. With Device No. 7, the transverse and longitudinal electrodes were kept insulated from each other, and separate electrical feedthroughs were brought out through the epoxy casting. This laser cavity was used to investigate the effects of different delay times between preionization pulse and longitudinal pumping pulse. It also made it possible to prevent the transverse discharge oscillations from modulating the longitudinal electrode voltage.

Attempts to line the discharge channel with glass (Devices 3 to 6) were primarily motivated by considerations concerned with eliminating chemical contamination of the gas mixture by materials outgassed from the epoxy surfaces. During their limited life span these glass systems showed no drastic improvements in laser performance (in comparison with the performance of Devices 2 and 7), however. On the other hand, the optical output from the epoxy devices could be increased by a factor of 2 to 5 by repeatedly "passivating" these discharge cavities with  $F_2$  (10 Torr for 2 hours) just prior to running each series of XeCl laser tests.

Best laser performance was achieved with Device No. 2, when excited with a circuit consisting of a 0.7 nF peaking capacitor and a pulse-sharpening rail gap. Highest laser output was 50 mJ with an intrinsic efficiency of 0.5 percent. The various discharge and circuit configurations tested are described in the following Sections 4.1 to 4.3.

TABLE 1. LTDD DEVICES BUILT AND TESTED

| DEVICE NO. | TRANSVERSE & LONGITUDINAL ELECTRODES (BRASS) | CONSTRUCTION   | FAILURE MODE   |
|------------|--|--|--|
| 1          | Common                                       | PVC plates cemented together.  | Electric breakdown along glued joints after 10 pulses.   |
| 2*         | Common                                       | Electrodes embedded in alumina-filled casting epoxy.   | Still operational after 50 000 pulses  |
| 3          | Separate                                     | Electrodes embedded in alumina-filled casting epoxy.   | Electric breakdown through 0.55-inch thick epoxy layer covering transverse electrodes after 10 pulses. |
| 4          | Separate                                     | Premachined MACOR glass panels cemented together. Electrodes and glass panels embedded in epoxy.             | MACOR fractured after two days due to mechanical stresses caused by shrinkage of epoxy.                |
| 5          | Separate                                     | 0.5-inch thick Pyrex panels epoxied together with electrodes attached.                                       | Failure of Pyrex due to combined mechanical and electric stresses after 50 pulses.                     |
| 6          | Separate                                     | 0.5-inch thick Pyrex panels cemented together. Electrodes potted separately in epoxy but not glued to Pyrex. | Pyrex fractured due to electrical breakdown after 100 pulses.  |
| 7*         | Separate                                     | Made from 0.75-inch thick NEMA-G10 glass-filled epoxy board embedded in casting epoxy mold.                  | Still operational after 10 000 pulses.   |

\*These devices did not fail even after lengthy service.



#### 4.1 Common-Electrode LTDD Device

The most successful LTDD unit built is shown in cross section in Figure 12. The electrodes were machined from  $\frac{1}{2}$ -inch thick brass bar with a full radius around all edges. The flat portions of the electrodes were 6.4 cm wide. The distance between the exposed ends of the electrodes, i.e., the length of the longitudinal discharge was 28 cm. The discharge channel was 2 cm high and 10 cm wide. The sides of the channel were shaped such that the electric field was close to normal to most of the dielectric surface (see Figure 12). This minimized surface tracking around the sides of the discharge channel. For the same reason, the channel was made considerably wider than the width of the gas volume preionized by the transverse discharge pulse.

The layer of dielectric, covering the major part of each electrode, was 1.4 cm thick. The material (Castall 302) was molded around the electrodes in four successive casting operations (Figure 12). Castall 302 is an alumina-filled ( $Al_2O_3$ ) electrical-grade epoxy with good casting properties and low shrinkage ( $2 \times 10^{-3}$ ). The dielectric strength of this material is listed as 3.98 kV/mil. Dielectric constant is 6.05. The capacitance of each dielectric layer, which was instrumental in coupling the transverse discharge energy into the gas; was approximately 46 pF per electrode.

Electrical connections were made by means of four  $\frac{1}{4}$ -inch diameter brass studs brought out through the cast epoxy from each electrode. NEMA G-10 plates, acting as high-voltage barriers, were epoxied to the sides and ends of the discharge cavity. Adjustable optical mounts were constructed entirely from insulating materials and were integrally attached to the end plates. The optical reflectors were 3-inch diameter optical quartz flats with multilayer dielectric coatings designed for 308 nm. Viton O-rings were employed as the gas seals between the reflectors and the discharge cavity.

##### 4.1.1 Direct Marx Drive

The first set of experiments were performed by connecting the high-voltage end of the Marx bank directly to one electrode of LTDD Device No. 2, using a 20-cm wide copper strap. A stable optical cavity was employed to extract the laser power. The total reflector had a 10 m radius of curvature (concave).

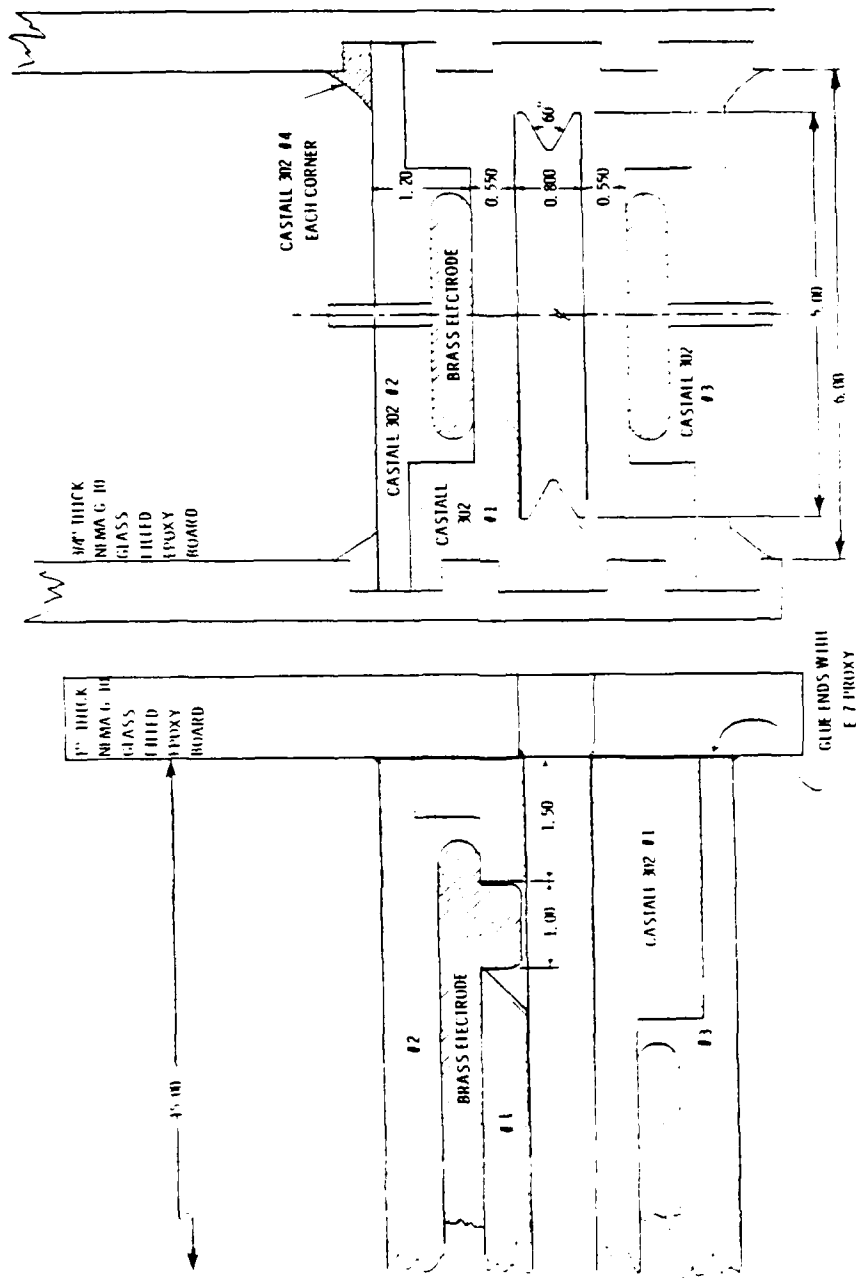


FIGURE 12. CONSTRUCTION OF LDD DEVICE WITH COMMON ELECTRODES

90 13

The output coupler was 80 percent reflective at 308 nm. Discharge current was measured with a Pearson coil around one of three ground return leads from the ITDD to the Marx generator. The optical pulse shapes were monitored with an ITT-F4000 vacuum photodiode with an S5 spectral response. Laser pulse energies were measured with a Gen-Tec pyroelectric energy meter. Marx charging voltages were between 30 and 40 kV per stage.

With gas mixtures of HCl, Xe and He, laser action was achieved on the B-X bands of XeCl at 308 nm. No lasing was observed when the device was operated with gas mixtures typical for KrF and XeF lasers using 70 percent output reflectors for 249 and 350 nm, respectively.

Uniform discharges and consistent lasing were observed for XeCl gas mixtures ranging from HCl/Xe/He = 0.02/1/1500 Torr to 1/5/1500 Torr. Optical pulse energies varied between 1 and 10 mJ. Note that these gas mixtures were much leaner in HCl and xenon than the optimum HCl/Xe/Ne mixtures of 3/90/3000 Torr employed with efficient e-beam excited XeCl lasers.<sup>1</sup>

In the present tests, the discharge deteriorated and lasing became intermittent when the partial pressures of HCl or Xe exceeded 2 or 5 Torr, respectively. Above 10 Torr of Xe pressure the glow disappeared almost completely. Instead, a bright arc was seen to bridge the discharge channel from the edge of the cathode to the opposite dielectric surface (Figure 13) and, after producing a complex branching pattern, appeared to track along this surface to the anode.

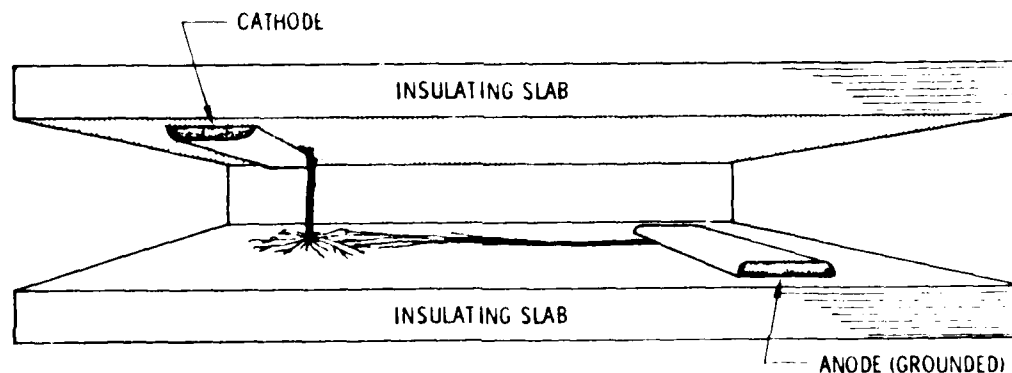


FIGURE 13. TYPICAL ARC PATTERN OBSERVED WHEN GAS MIXTURE IS TOO RICH IN XENON

Measured current and laser power as a function of time are reproduced in Figure 14. Gas mixture was HCl/Xe/He = 0.3/3/1500 Torr, and the Marx charging voltage was 40 kV. Note that the current pulse exhibited only a 30 percent reversal and that the damping was quite good. This indicates, that even with a high circuit inductance, the discharge impedance was fairly well matched to the circuit. From the ringing period  $\tau$  of the discharge current, the total circuit inductance  $L$  can be calculated from

$$L = \frac{\tau^2}{4 \pi^2 C} \quad (4.1)$$

The observed ringing period indicates a value for the Marx inductance plus the inductance of the connections to the LTDD of  $3 \mu\text{H}$ , which is very large. No transverse-discharge rare-gas halide laser can be made to work with so high a circuit inductance. The characteristic circuit impedance

$$Z = \sqrt{L/C} \quad (4.2)$$

works out to be approximately 80 ohms here, so that the discharge impedance must have been on the order of 50 ohms. The width (FWHM) of the main current pulse was 75 ns. The width of the laser pulse was approximately 55 ns (Figure 14). The ripple seen on the current trace is believed to be due to transverse oscillations coupled through the dielectric layer on the electrodes ( $C = 5$  to  $20 \text{ pF}$ ). Owing to the much lower discharge impedance in the transverse direction ( $\sim 0.5 \dots$ ), this circuit is very much underdamped. The transverse excitation mode can therefore be considered equivalent to RF-excitation at 30 MHz.

#### 4.1.2 Pulse-Forming Networks

The common-electrode LTDD was tested with a number of pulse-forming network configurations. Only a limited number of circuit arrangements proved useful. These consisted primarily of simple peaking circuits with and without pulse-sharpening spark gaps. Successful circuit configurations are summarized in Figure 15.

Note the location of the Pearson-type current probes in various branches of the circuit. A purely resistive branch (copper-sulfate resistor) was added to

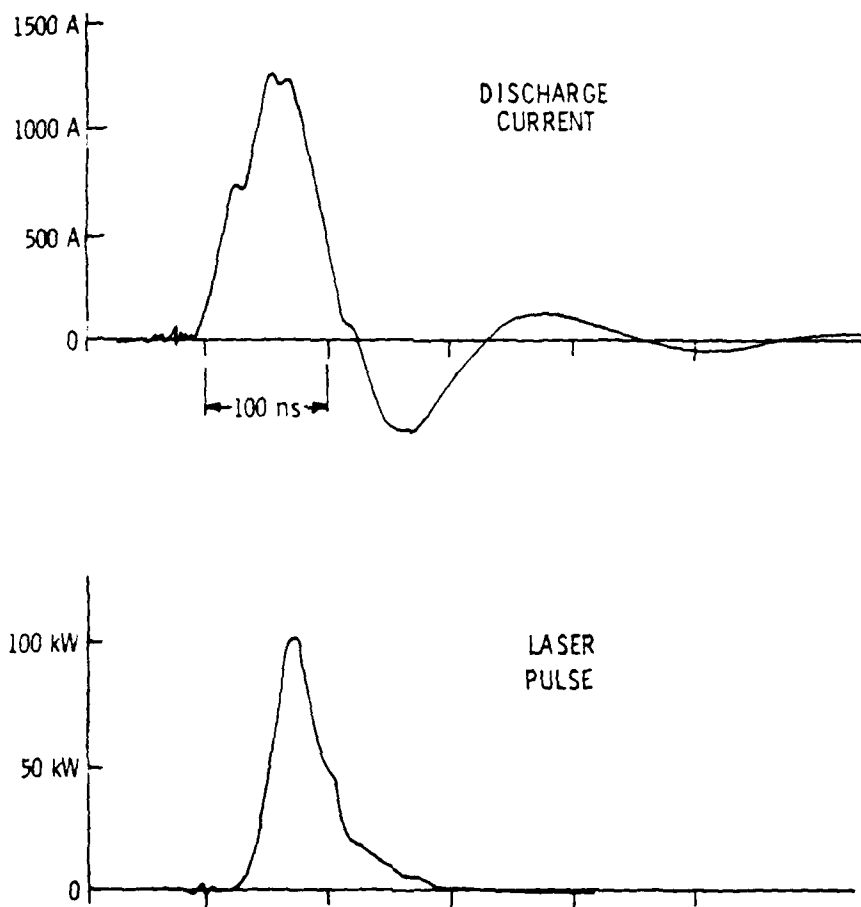


FIGURE 14. CURRENT AND LASER PULSE FOR MARX BANK (CONF. A)  
FEEDING LTDD DIRECTLY ( $V_{CH} = 40$  kV)

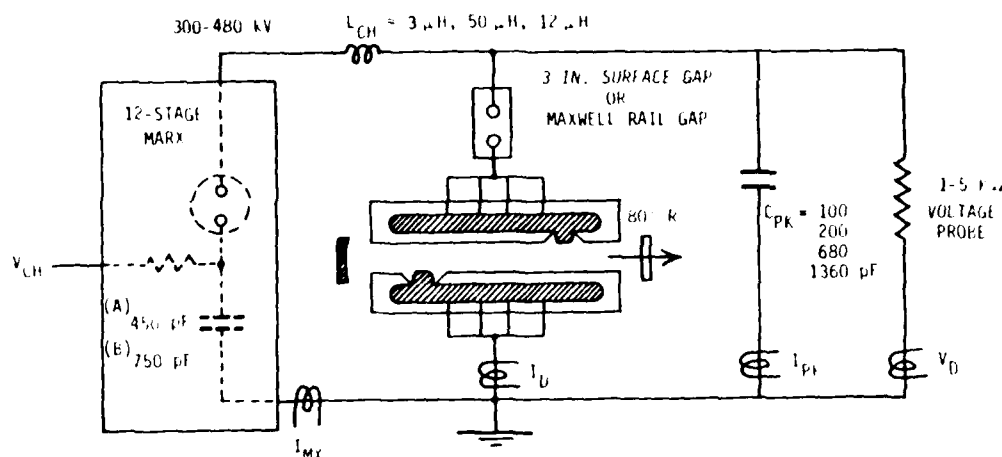


FIGURE 15. ELECTRIC PULSE GENERATOR FOR TLDD LASER

measure the voltage pulse ( $V_D$ ). The resistance of this diagnostic branch was either 1 k $\Omega$  or 5 k $\Omega$ , depending on the lowest resistance that could be tolerated with the circuit (and the discharge impedance) without disturbing the circuit response. Voltages were calculated from the current in this branch measured with a Pearson coil.

Results of a comprehensive study, in which all circuit and discharge parameters were systematically varied, will now be described in the following subsections.

#### 4.1.2.1 Peaking Capacitor Without Pulse-Sharpening Gap

The addition of a simple peaking capacitor increased the optical pulse energy from less than 10 mJ to 15 mJ. Furthermore, these higher output energies could be obtained with lower Marx charging voltages (in the range of 22 to 28 kV). This more than doubled the overall efficiency of the system from 0.025 to 0.06 percent. The laser performance was not strongly dependent on the size of the

peaking capacitor. Best pulse energies were obtained with a 680 pF capacitor, although other capacitors in the range between 100 pF and 1.4 nF worked almost as well.

Uniform glow discharges could now be produced with a wider range of gas mixtures, than before, but were still limited to xenon partial pressures of less than 10 Torr. It was also found that other chlorine donors, such as  $\text{CCl}_4$  and  $\text{BCl}_3$ , gave essentially the same optical output pulses when the corresponding gas mixtures were optimized. For a simple 100 pF peaking circuit, the optimum gas mixtures were

$$\text{HCl/Xe/He} = 0.5/4/1500 \text{ Torr}$$

$$\text{CCl}_4/\text{Xe/He} = 0.1/1/1500 \text{ Torr}$$

and

$$\text{BCl}_3/\text{Xe/He} = 0.1/1/2500 \text{ Torr}.$$

Results of a parametric study of output versus gas mixture is described in more detail for a different circuit configuration in a later section of this report. Substitution of neon in place of the helium for the prime diluent produced less stable discharges with no increase in optical output power.

For a typical laser mixture of  $\text{CCl}_4/\text{Xe/He} = 0.1/1/2000$  Torr and a 100 pF peaking capacitor, the discharge circuit characteristics and optical output pulse have been replotted in Figure 16. The voltages and currents showed a complex pattern of oscillations which was a result of the interaction between transverse and longitudinal discharge paths, the peaking circuit and the Marx bank network. No isolation coil was used between the Marx bank and the peaking capacitor, so that the Marx circuit could continue to feed energy into the gas after the initial discharge of the peaking capacitor. This accounts for the wide  $I_D$  pulse. Study of the  $V_D$ ,  $I_D$  and  $I_{PK}$  traces makes it possible to reconstruct the initial sequence of events as follows.

During the first 30 ns the Marx bank transfers charge into the peaking capacitor (positive cycle of  $I_{PK}$  curve), and the voltage  $V_D$  rises to approximately 250 kV. At this point in time, while the peaking capacitor is still being charged, the transverse predischage takes place. Evidence of this are the

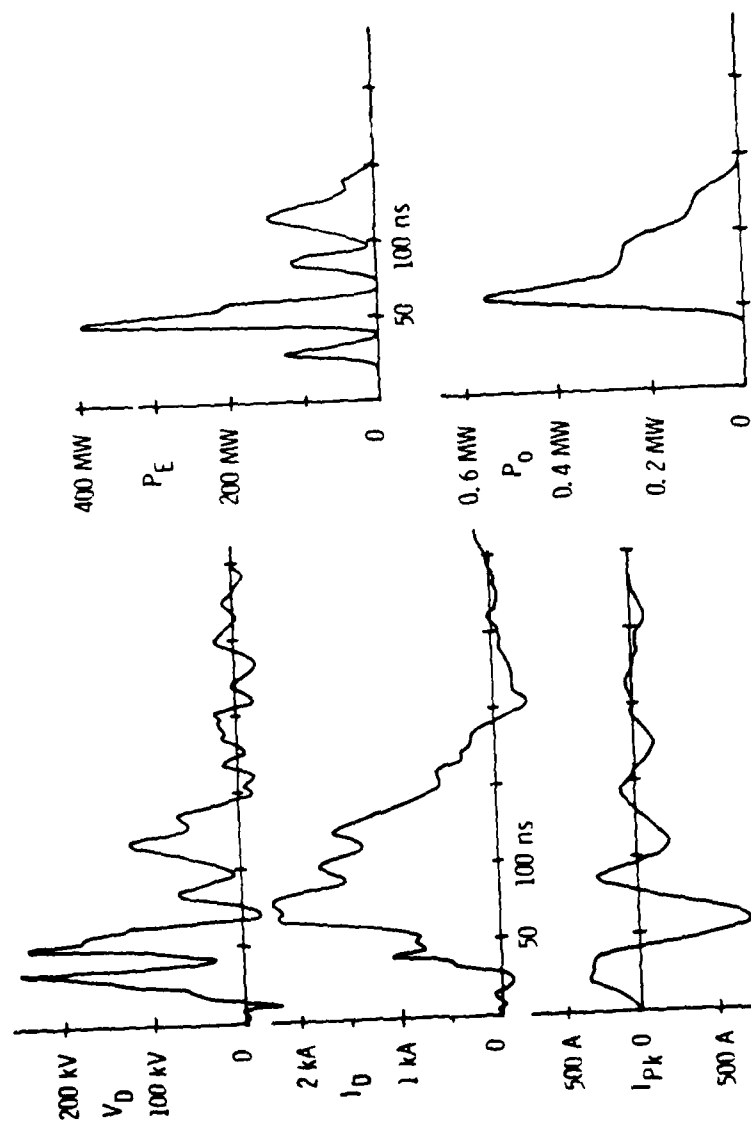


FIGURE 16. PULSE SHAPES OF DISCHARGE VOLTAGE ( $V_D$ ) AND CURRENT ( $I_D$ ), CURRENT IN PEAKING CIRCUIT ( $I_{pk}$ ), ELECTRIC POWER DEPOSITED IN DISCHARGE ( $P_E$ ), AND OPTICAL POWER ( $P_o$ ).



first narrow current spike detected by the  $I_D$  coil and the momentary drop in voltage on the electrodes. After the short pulse of the transverse displacement current has charged up the surfaces of the dielectric walls of the discharge channel, the voltage recovers very quickly and initiates the longitudinal discharge. The current is now draining out of the peaking capacitor (negative excursion of  $I_{PK}$ ) into the discharge (high peak of  $I_D$ ). As the peaking-circuit current oscillates with decreasing amplitude, current from the Marx generator keeps the discharge current positive.

The electrical power deposited in the laser gas can be calculated by multiplying the values of  $V_D$  and  $I_D$  at each instant of time. The resulting power deposition curve is shown in the upper right diagram of Figure 16. Note that there are four separate power input peaks: the first due to the transverse preionization pulse, the second due to the peaking capacitor dumping its energy into the longitudinal discharge (primary pumping pulse), and the third and fourth peaks due to subsequent oscillations in the peaking circuit.

The prepulse does not pump the gas up to lasing threshold conditions. However, all three longitudinal power input pulses are reflected in the laser pulse ( $P_O$ ), which has a total base width of over 100 ns here. This state of affairs suggests the possibility of producing an extra long XeCl laser pulse with a high-frequency oscillating pump pulse. In a parallel independent R&D program,<sup>25</sup> an XeCl laser pulse of more than 200 ns half width has been produced by pumping a transverse discharge (Figures 3 and 4) with an oscillating power input pulse. In the latter experiment the discharge current actually reversed periodically at a frequency of 20 MHz.

The well-defined oscillations observed in the peaking circuit (Figure 16) can be utilized for calculating a characteristic discharge impedance. For a series RLC circuit the current is given as a function of time by

$$I = \frac{2V_0}{R\sqrt{4\lambda^2 - 1}} e^{-\frac{Rt}{2L}} \sin\left(\frac{Rt}{2L} \sqrt{4\lambda^2 - 1}\right) \quad (4.3)$$

where

$$\lambda = \sqrt{L/C} / R.$$

If the circuit is severely underdamped,  $4\lambda^2 \gg 1$  and

$$\sqrt{4\lambda^2 - 1} \approx \frac{2}{R} \sqrt{\frac{L}{C}} \quad (4.4)$$

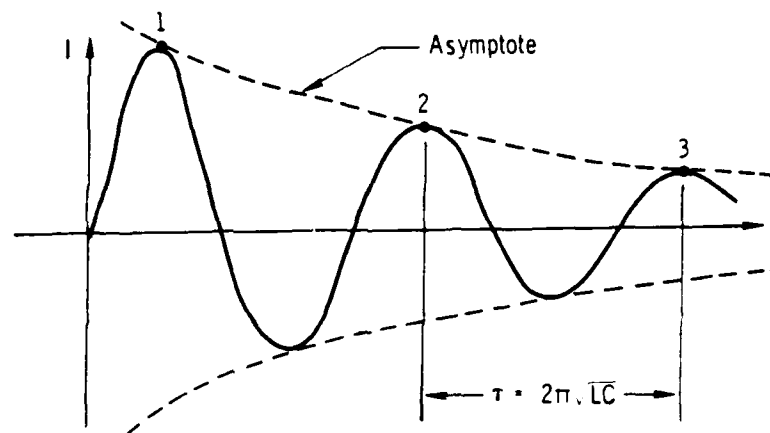


FIGURE 17. CURRENT OSCILLATIONS IN AN UNDERDAMPED RLC CIRCUIT

The equation of the asymptote (Figure 17) connecting the oscillation peaks is then given by

$$I_{\text{asym}} = V_0 \sqrt{\frac{C}{L}} e^{-\frac{Rt}{2L}} \quad (4.5)$$

which expresses the exponential rate of decay of the amplitude of the current oscillations. Hence

$$\frac{I_2 - I_1}{\tau} = -\frac{R}{2L} \quad (4.6)$$

But the period of oscillation is

$$\tau = 2\pi \sqrt{LC} \quad (4.7)$$

so that Equation (4.6) can be rewritten as

$$R = \frac{1}{\pi} \sqrt{\frac{L}{C}} \cdot \frac{I_1}{I_2} = \frac{\tau}{2\pi^2 C} \cdot \frac{I_1}{I_2} \quad (4.8)$$

For the peaking circuit  $C = C_{PK}$  and  $R = R_D$ , since the discharge can be considered to be the only resistive element (dissipative) in the circuit. By measuring two successive current peaks ( $I_1$  and  $I_2$ ) and the oscillation period ( $\tau$ ), the discharge impedance can thus be determined from Equation (4.8). Figure 18 shows the peaking current as a function of time for a number of different gas mixtures in the discharge. For all runs, the ratio of  $CCl_4/Xe$  was the same, but the gas mixtures were made more dilute in going from (a) to (d). Applying Equation (4.8) to these current profiles shows that the discharge impedance increased from 16 .. to 90 .. as the xenon concentration was dropped from 15 Torr to 0.7 Torr. The discharge impedance for a typical laser mixture (c) is therefore indeed around 50 ohms for the longitudinal discharge. This compares with 1 ohm observed in a conventional TE-laser (Figure 5).

#### 4.1.2.2 Construction of Pulse-Sharpening Surface Gaps

With the simple peaking circuits described above, the voltage rise time at the electrodes was observed to be approximately 20 ns and the peak electrode voltage was about 250 kV. This is less than half the maximum voltage that can theoretically be reached in the peaking circuit, if the gas breakdown in the laser cavity could be delayed. One way to achieve a more highly overvolted discharge pulse is to insert a pulse-sharpening rail gap between the peaking capacitor and the discharge electrode (Figure 15).

In order to decrease the voltage rise time and increase the initial electrode voltage, a 300 kV rail gap was required. The first gap tested was a multi-channel surface gap designed and built according to data obtained from Reference 22. It was a double-sided surface gap, made by etching a copper-clad printed circuit board (NEMA G-10 substrate) on both sides as shown in Figure 19. Two electrode profiles were tried. Electrode shape A was flat with rounded corners, and the electrode gap was 4 inches. It performed poorly, insofar that only one arc channel was observed at one or the other end. The second version (electrode shape B) had a Bruce<sup>26</sup> profile and a 3 inch electrode gap. When this gap was operated as a pulse-sharpening spark gap (see Figure 15

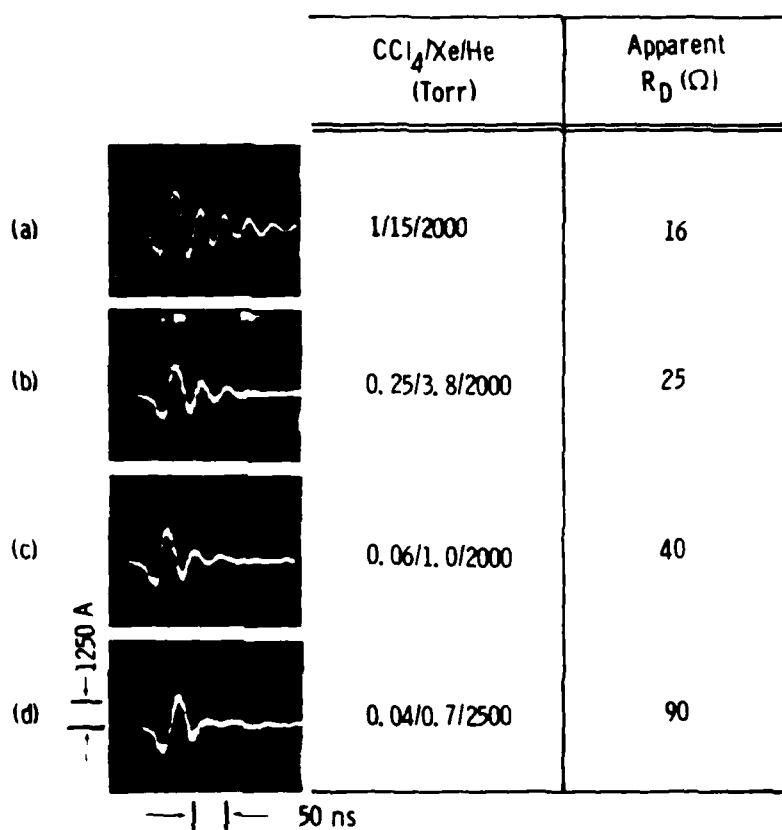


FIGURE 18. CURRENT OSCILLATIONS IN PEAKING CIRCUIT ( $C_{PK} = 100 \text{ pF}$ ) AS A FUNCTION OF LASER GAS MIXTURE

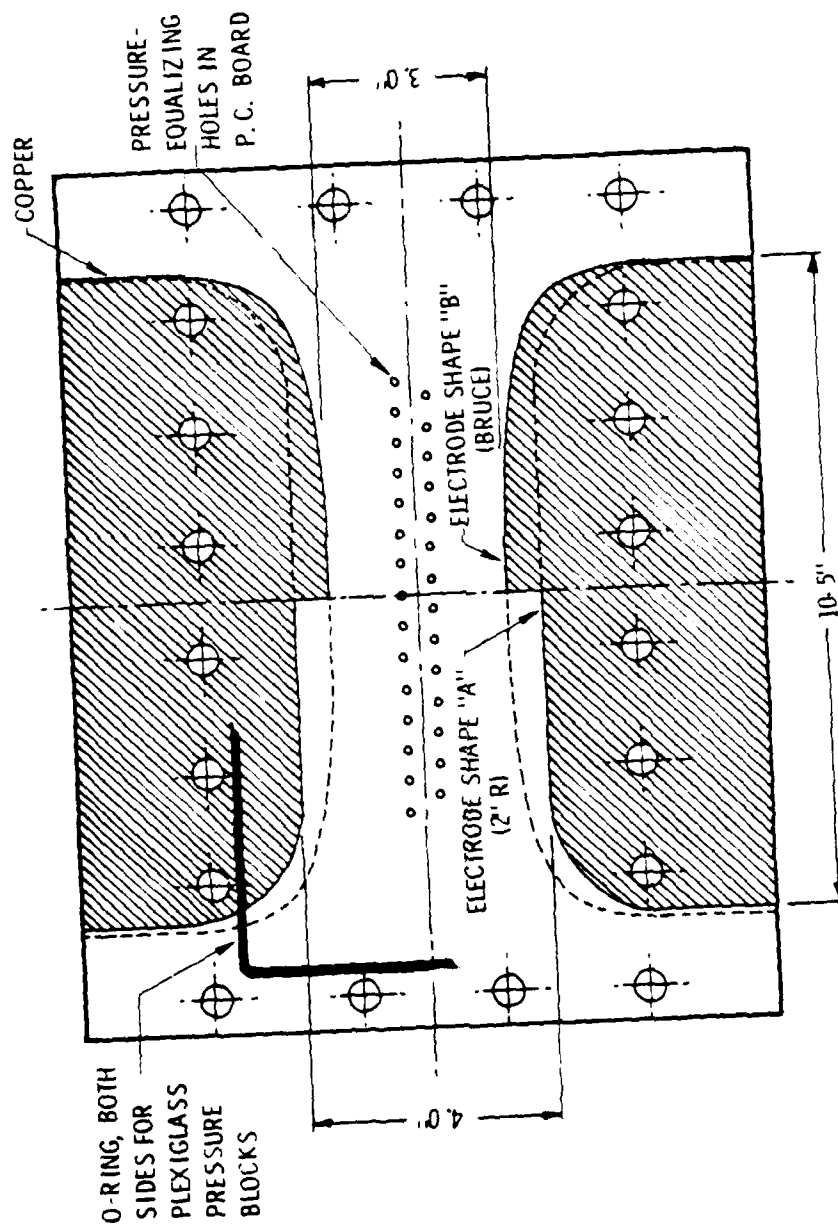


FIGURE 19. ELECTRODE SHAPES OF SURFACE-SPARK GAPS TESTED.

for location in circuit), three to four arc channels were generally observed at random positions. A large number of tests were performed with this surface gap. To permit pressurization of this double-sided surface gap, the printed circuit board was sandwiched between two hollow plexiglass pressure blocks and sealed with O-rings.

#### 4.1.2.3 Peaking Capacitor with Pulse-Sharpening Gap

With the addition of a pulse-sharpening gap, lasing could be achieved more consistently than before over a wider range of gas mixtures and pressures. Consistent lasing occurred over a range of xenon partial pressures from 0.2 to 10 Torr and with total pressures (He diluent) between 400 and 2000 Torr.

Highest laser powers were obtained with a 0.68 nF peaking capacitor and with 35 to 40 psi of an Ar/N<sub>2</sub> mixture (90%/10%) in the surface gap. The surface gap did not work well in air or nitrogen. In some of the later tests the surface gap was replaced by a Maxwell rail gap made from 1-inch diameter brass rods spaced approximately 19 mm apart. The rail gap could be used with nitrogen, air or Ar/N<sub>2</sub> mixtures. Use of the rail gap in place of the surface gap resulted in a 20 percent increase in optical output.

It was also found advantageous to isolate the peaking circuit from the Marx bank with a 12  $\mu$ H charging coil ( $L_{CH}$ ). This prevented any charge on the peaking capacitor from ringing back into the Marx during the laser excitation period.

With the Marx bank in configuration A, with a 680 pF peaking capacitor and the 3-inch surface gap, best laser output energy was approximately 20 mJ. When the surface gap was replaced with a rail gap, the optical pulse energy went up into the 25 to 30 mJ range. This corresponds to an overall efficiency of circa 0.1 percent. With the Marx bank in configuration B, output increased to 50 mJ, but efficiency stayed the same.

With either type of spark gap it was no longer possible to obtain a reliable voltage pulse measurement, because the RF noise emanating from the spark gap was picked up by the voltage probe and the oscilloscope and could not be filtered out. Typical current pulses measured with this circuit configuration

are reproduced in Figure 20A and 20B. Note the 280-ns long charge-transfer pulse in the  $I_{PK}$  trace, followed by the 70-ns wide discharge pulse (negative in Figure 20A and positive in Figure 20B). The transverse prepulse is clearly distinguishable in the discharge current  $I_D$  as a fast spike 20 ns ahead of the peak of the main discharge pulse. Figure 20C shows the corresponding laser pulse, which is 50 ns wide here.

The dependence of optical pulse energy on charging voltage is plotted in Figure 21. Note that the output energy increases approximately linearly with charging voltage. This is consistent with the energy stored in the Marx bank being also approximately linear with voltage (see Figure 10). The gas pressure in the pulse-sharpening gap was adjusted in direct proportion to the charging voltage. This was necessary to make certain that the peaking capacitor was fully charged before the rail gap broke down to initiate the discharge sequence.

At lower rail gap pressures, the discharge drained the peaking capacitor at a time when the charge transfer was not yet complete. The amount of electrical energy dumped into the discharge could therefore be controlled by adjusting the gap pressure. Figure 22 shows what happened to the optical output pulse as the energy in the pumping pulse was varied in this manner. The peaking capacitor voltages ( $V_{PK}$ ) are estimated values only, and were taken to be proportional to the gas pressure in the rail gap.  $E_{EL}$  is the energy stored in the peaking capacitor just before breakdown of the spark gap. The optical pulse shapes were obtained with an F 4000 vacuum photodiode (S5 spectral response) with an aperture equal to the cross section of the laser beam.  $E_0$  is the time integral of the recorded optical power pulse.

When the pump pulse contained less than 6 joules, the gas excitation was below lasing threshold. Accordingly, only fluorescence was observed, of which merely a small fraction was collected by the diode. The slow 100 ns rise on the fluorescence pulse was wider than the pumping pulse and probably indicates that there is a slow rate-limiting reaction in the formation kinetics leading to excited  $XeCl^*$  molecules. With 8.7 J (30 J/μ) switched into the discharge (center oscillogram in Figure 22) the excitation level has just passed lasing threshold, and the beginning of a laser pulse can be seen growing out of the tail of the fluorescence pulse. With 20 J switched into the gas (bottom photograph) the laser pulse is fully developed, showing the characteristic fast

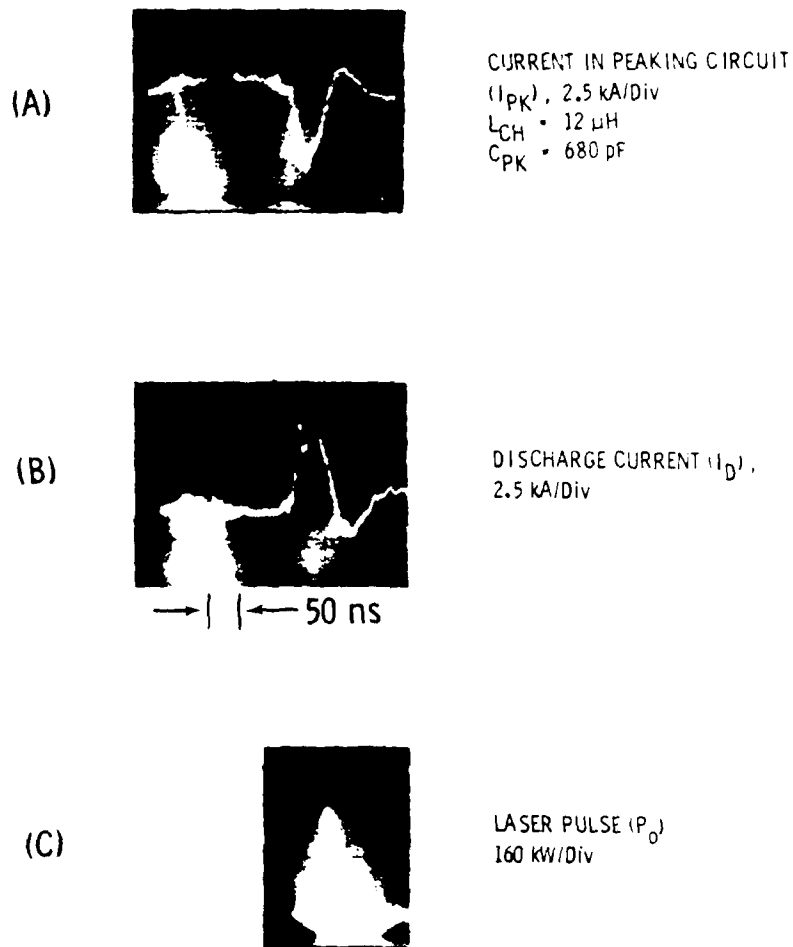


FIGURE 20. PEAKING-CIRCUIT CURRENT (A), DISCHARGE CURRENT (B), AND OPTICAL LASER POWER (C) WITH PULSE-SHARPENING RAIL GAP (39 PSI AIR) AND 30 kV MARX CHARGING VOLTAGE. GAS MIXTURE:  $HCl/Xe/He = 1/6/2600$  TORR

80-14



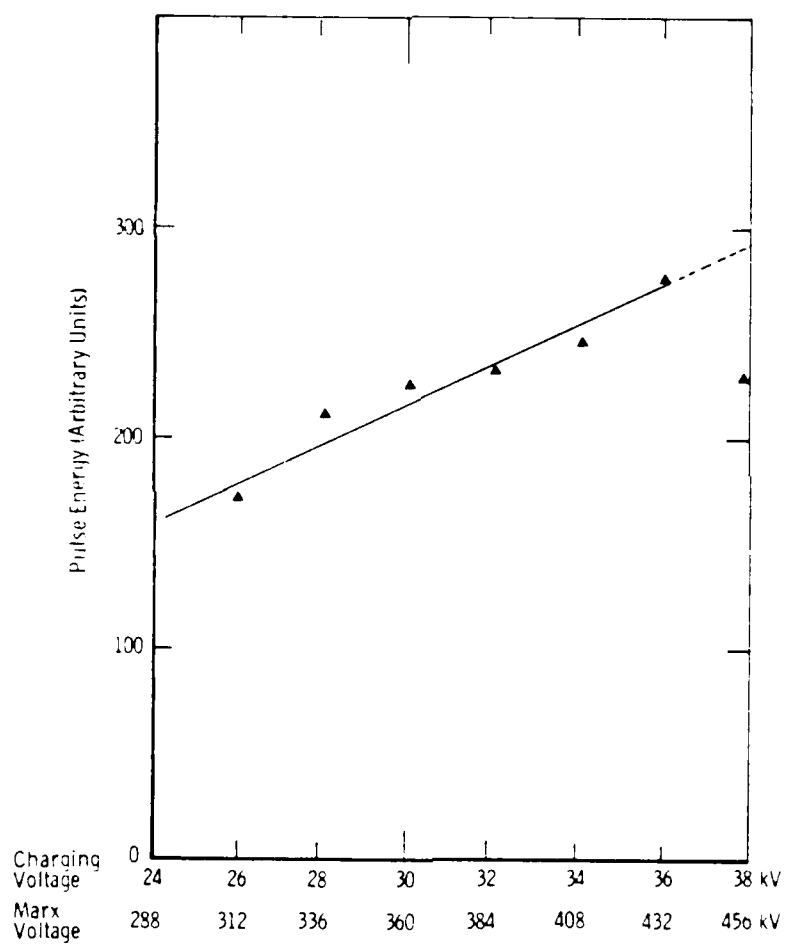


FIGURE 21. OPTICAL PULSE ENERGY AS A FUNCTION OF CHARGING VOLTAGE (GAS MIXTURE:  $\text{HCl}/\text{Xe}/\text{He} = 0.5/3/2600$  Torr)

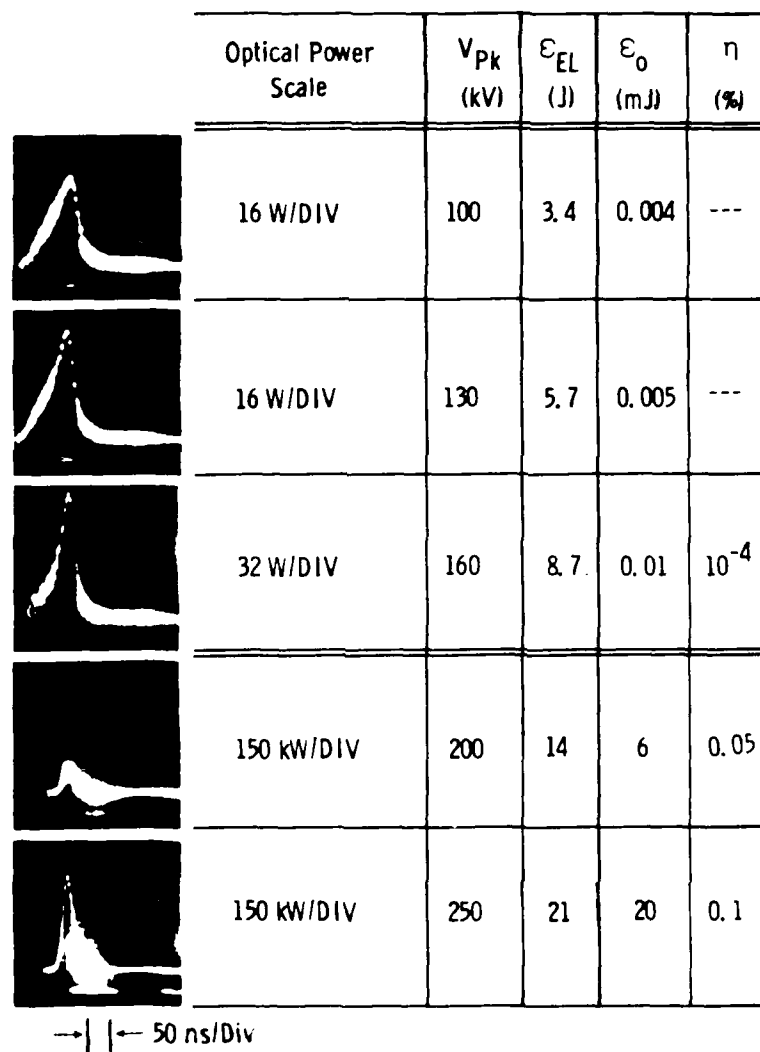


FIGURE 22 EVOLUTION OF OPTICAL PULSE ( $\epsilon_o$ ) FROM FLUORESCENCE  
TO LASING WITH INCREASING ELECTRIC ENERGY ( $\epsilon_{EL}$ ) INPUT

rise time of a gain-switched pulse. The last column in Figure 22 gives the electrical laser efficiency based on energy switched into the discharge load.

Figures 23 to 25 give the results of a comprehensive study of the LTDD performance as a function of gas mixture. These tests were performed with a 100 pF peaking capacitor and with the 3-inch surface gap. The Marx bank was in configuration A. The diluent was helium at a pressure of approximately 1300 Torr.

Figure 23 shows the optical pulse energy plotted against partial pressure of the chlorine donor, which was  $\text{CCl}_4$  here. Each curve corresponds to a different concentration ratio of xenon to carbon tetrachloride. Note that at higher  $\text{Xe}/\text{CCl}_4$  ratios the curves peak at lower partial pressure of  $\text{CCl}_4$ . Highest output was achieved with an  $\text{Xe}/\text{CCl}_4$  ratio of 24 at a  $\text{CCl}_4$  pressure of 0.15 Torr (Xe pressure of 3.6 Torr).

With HCl as the chlorine donor best output was obtained with a relatively low  $\text{Xe}/\text{HCl}$  ratio of 2.5 at an HCl partial pressure of 0.6 Torr (Xe pressure of 1.5 Torr). Note that under optimum conditions the number of available Cl atoms were the same ( $2.1 \times 10^{16} \text{ cm}^{-3}$ ) for both chlorine donors. For different  $\text{Xe}/\text{HCl}$  ratios, however, the peaks of the energy curves were spread out over an entire order of magnitude of HCl concentrations (see Figure 24). This suggested that the laser performance was more strongly determined by the xenon concentration rather than HCl concentration. When the data were replotted against partial pressure of xenon, it became evident that all curves peaked at xenon pressures of approximately 1.8 Torr, independent of  $\text{Xe}/\text{HCl}$  ratio (see Figure 25).

This observation is at odds with theory for electron attachment-dominated discharges. The theory would predict that a higher HCl concentration should be more effective in preventing ionization instabilities (due to two-step ionization of xenon) and should permit higher xenon concentrations. At approximately twice the total pressure (2600 Torr He) a similar set of tests showed that the optimum xenon pressure was about 5 Torr under those conditions. This is still well below the optimum partial pressures of xenon (close to 100 Torr) found for e-beam excitation<sup>1</sup> of XeCl laser mixtures.

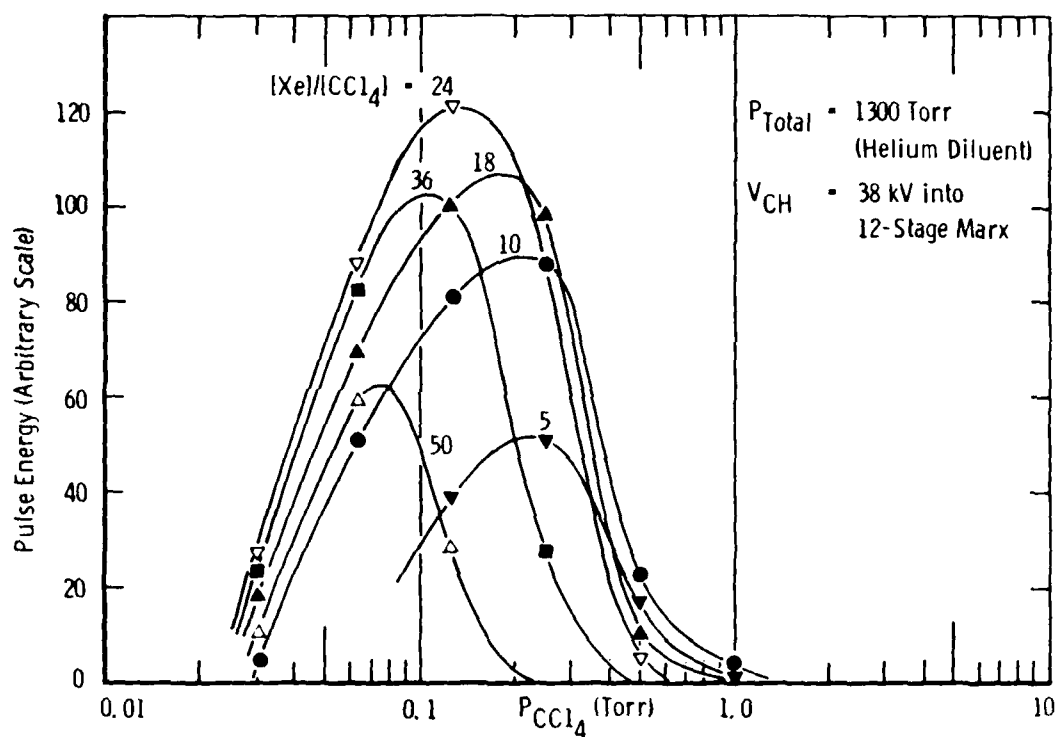


Figure 23. OPTICAL PULSE ENERGY AS A FUNCTION OF  $CCl_4$  PARTIAL PRESSURE AND  $Xe/CCl_4$  RATIO FOR  $Xe/CCl_4/He$  MIXTURES AT 1300 TORR TOTAL PRESSURE

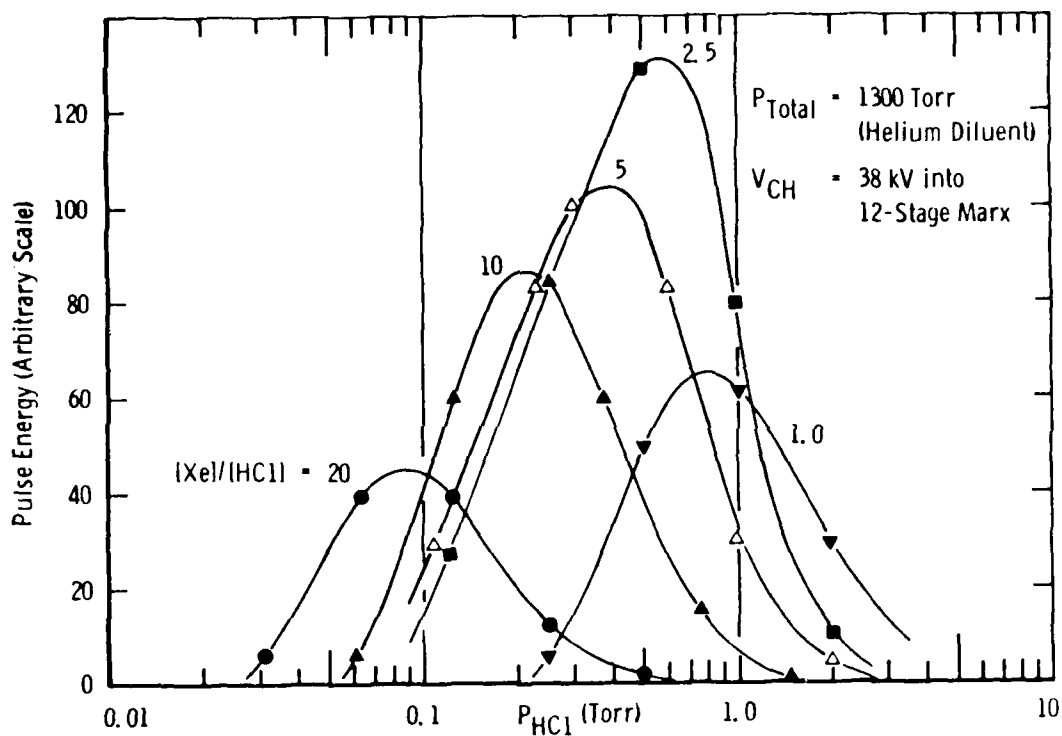


Figure 24. OPTICAL PULSE ENERGY AS A FUNCTION OF HCl PARTIAL PRESSURE  
 AND Xe/HCl RATIO FOR Xe/HCl/He MIXTURES AT 1300 TORR TOTAL  
 PRESSURE

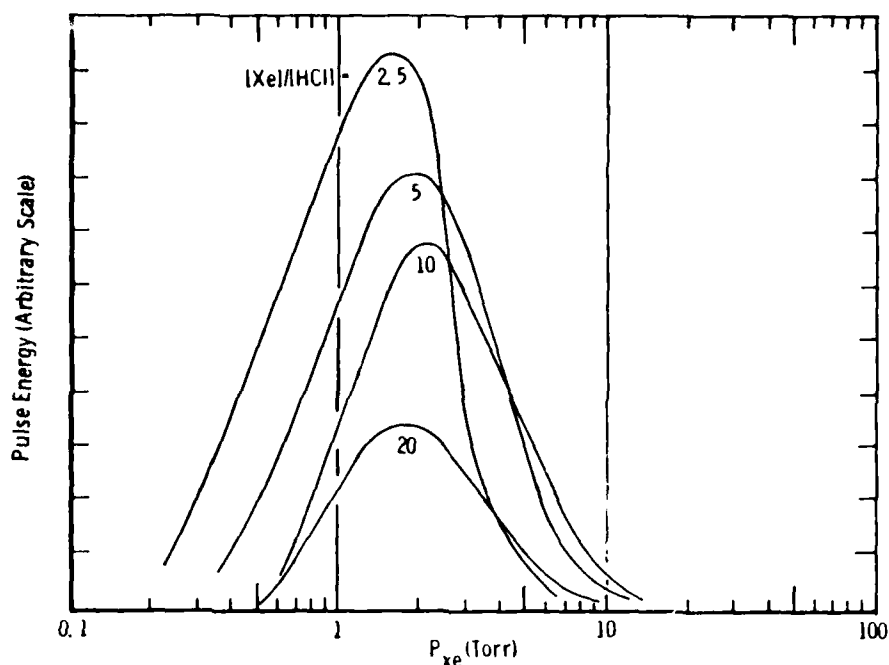


FIGURE 25. OPTICAL PULSE ENERGY AS A FUNCTION OF Xe PARTIAL PRESSURE AND Xe/HCl RATIO FOR Xe/HCl/He MIXTURES AT 1300 Torr TOTAL PRESSURE

86-17

It appears therefore that the electrical efficiencies attainable with a longitudinal XeCl laser are limited to relatively low values, because at the high xenon concentrations, necessary for fast production of XeCl excited states, the laser discharge shows signs of instability due to tracking along the insulator surfaces.

#### 4.2 Separate-Electrode LTDD Device

Device No. 7 (see Table 1) was constructed essentially the same as Device No. 2 (described in Figure 12), except that separate sets of brass electrodes were used for the transverse and longitudinal discharge excitation. The transverse electrodes were 20 cm long and were totally embedded in alumina-filled epoxy. The insulating slab between each transverse electrode and the discharge channel was a 19-mm thick NEMA G-10 glass-filled epoxy board. The distance between exposed end electrodes was 28 cm as before. Under the most favorable conditions (minimum delay between transverse and longitudinal discharge pulses),

laser output from this discharge chamber was approximately 50 percent of the best output obtained from Device No. 2.

Discharge circuits in which the transverse and longitudinal discharges were excited from separate independently triggered pulse generators proved unworkable. The relatively high values of time jitter involved in triggering extra-high voltages ( $> 200$  kV) made it impossible to define the delay between the two discharges with an accuracy of better than  $\pm 100$  ns. This experimental difficulty precluded the use of delay times of less than 100 ns. At delays of 200 ns or longer, no lasing was observed under otherwise favorable conditions (optimum gas mixture, pressure, pulse shape, pulse energy, etc.). With short delay times ( $< 100$  ns), the lack of control over the exact timing of the discharge pulses led to the early destruction of some of the discharge chambers (Table 1), because the longitudinal discharge pulse occurred first without preionization of the gas. This condition favors electrical insulation breakdown, due to arcing between the "live" end electrode and the encapsulated transverse ground electrode.

The more successful circuits were variations of the circuit shown in Figure 26. A passive delay between the two discharges was generated here by employing LC networks with variable inductance ( $L_D$ ) and rail gaps, whose breakdown potential could be varied by adjusting the gas in the spark gaps. With this type of network the preionization capacitor  $C_T$  was charged directly from the Marx bank with a maximum charging period of  $\pi \sqrt{L_{MX} C_T} = 100$  ns. The pressure in rail gap A was set so that it broke down at the desired transverse discharge voltage. With gap A conducting, some of the energy in  $C_T$  was conducted into the transverse discharge. The remaining electric charge was transferred to the longitudinal discharge capacitor  $C_L$  in a time period

$$\tau_L = \pi \left( \frac{L_D C_T C_L}{C_T + C_L} \right)^{1/2} \quad (4.9)$$

Charging of  $C_L$  was supplemented by current from the Marx bank at a somewhat slower rate. The delay time and longitudinal discharge voltage were varied by adjusting  $L_D$ ,  $C_L$  and the pressure in rail gap B. During the experiments it was found that rail gap A could be omitted (shorted) without seriously affecting laser performance.

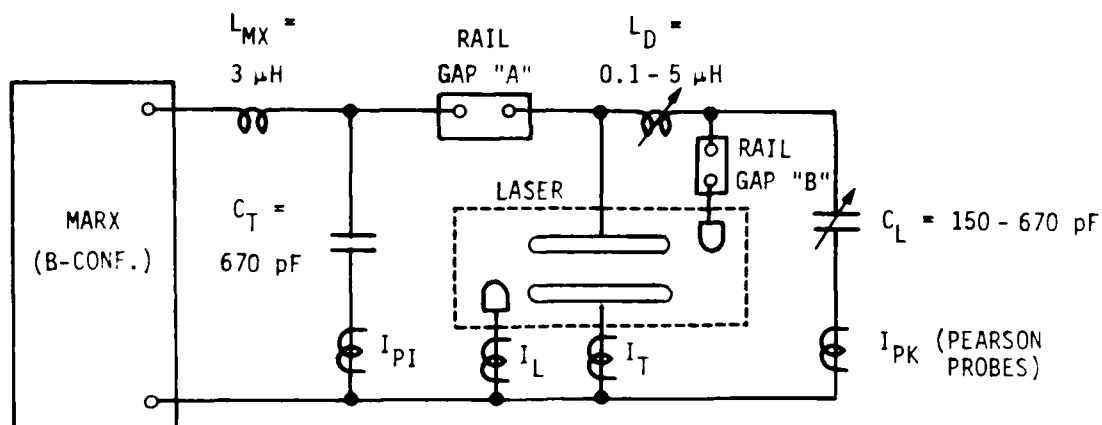


FIGURE 26. TYPICAL DOUBLE-DISCHARGE CIRCUIT WITH PASSIVE DELAY FOR SEPARATE-ELECTRODE DEVICE

Careful testing of the separate-electrode configuration showed that best performance was achieved when the period between discharge pulses was minimized by making  $L_D$  small. No lasing occurred when  $\tau_L$  was larger than 50 ns. Optimization of the circuit parameters led in fact to the same configuration (with transverse and longitudinal electrodes essentially tied together) which proved optimal for the common-electrode device.

#### 4.3 Variations in Discharge Geometry

After completion of the tests described in Section 4.2, Devices No. 7 and 2 were modified to investigate the effects of decreasing the longitudinal discharge length and of decreasing the height of the discharge channel.

The discharge length was decreased from 28 cm to 10 cm ( $E/N$  value more than doubled) by removing the end electrodes from Device No. 7 and by substituting two electrodes running along the sides of the discharge cavity.

The channel height was reduced from 20 mm to 3 mm by inserting additional dielectric slabs over the transverse discharge electrodes in Device No. 2. Both changes resulted in poor discharges and no laser output.



#### 4.4 Effects of Gas Additives

One might expect that the introduction of certain additives may favorably affect the laser performance, such as:

1. The introduction of trace amounts of easily ionizable species (xylene, tri-n-propylamine) may improve preionization.
2. The use of prime diluents other than helium (neon, argon) changes the gas breakdown potential and the mean energy of the discharge electrons.
3. The addition of gases which produce large amounts of vacuum-uv ( $N_2$ ) may make the discharge more uniform. The introduction of vibrationally excited species may be expected to also influence the discharge impedance and the formation and de-excitation reactions of species important to the lasing kinetics.
4. The addition of strongly attaching halogen compounds ( $F_2$ ,  $C_2F_6$ ,  $NF_3$ ) may stabilize the discharge by preventing ionization runaway.

The results of tests, in which varying concentrations of xylene, Ne,  $N_2$  and  $C_2F_6$  were added to the basic gas mixture, can be summarized as follows:

1. Addition of approximately 0.1 Torr xylene increased output by 10 percent.
2. Replacement of some or all of the helium diluent by neon or argon did not improve the output, but appeared to cause a deterioration of the discharge uniformity.
3. Addition of 20 Torr of  $N_2$  reduced laser output to zero.
4. Addition of 0.5 Torr of  $C_2F_6$  reduced laser output 50 percent.

Whereas small amounts of xylene proved beneficial, almost all molecular gases acted as effective quenchants.

## 5.0 THEORETICAL ANALYSIS

In support of the experimental program a theoretical model was developed to describe the interaction between discharge and external circuit. The objective was to maximize the power transfer into the laser gas by tailoring the circuit to match the time-varying discharge impedance. The initial approach has been to define the simplest possible circuit and discharge model which reflects the major features of the experimental data and to characterize the dependence of discharge power on circuit parameters. Results of some sample calculations are described in Section 5.1. Results of a separate study of the discharge and chemical kinetics of the XeCl laser are given in Section 5.2.

### 5.1 Circuit and Discharge Modeling

The model consists of a set of coupled differential equations describing the external circuit and the discharge kinetics. The circuits considered here are single- and two-stage LC networks switched directly across the discharge. Addition of a series peaking switch is straightforward. The discharge is initiated with a uniform charge density at  $t = 0$ . The circuit elements are lumped into equivalent resistors, capacitors and inductors with fixed values while the discharge resistance is determined by the charge density and electron mobility. Kinetic processes included in the model are single- and two-step ionization, dissociative attachment, electron and ion recombination, and metastable production and quenching. The calculation of rate constants and a detailed discussion of kinetics is given in Section 5.2.

First, let us consider the single-stage LC network shown in Figure 27. The inductance of the switch and of the discharge chamber are combined in  $L$ . The capacitor is initially charged to  $V_0$ . The discharge itself is a simple transverse or longitudinal electrode geometry containing a typical KrF laser gas mixture. The discharge voltage and current waveforms are shown in Figure 28. The switch is assumed to close instantaneously, so that the voltage rise time is limited by  $L/R_0$ , where  $R_0$  is the initial discharge resistance. In an actual device the rise time is limited by the switch closing time.

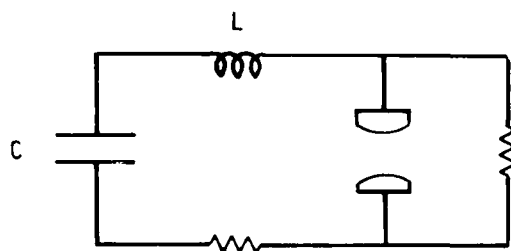


FIGURE 27. ONE-STAGE PFN

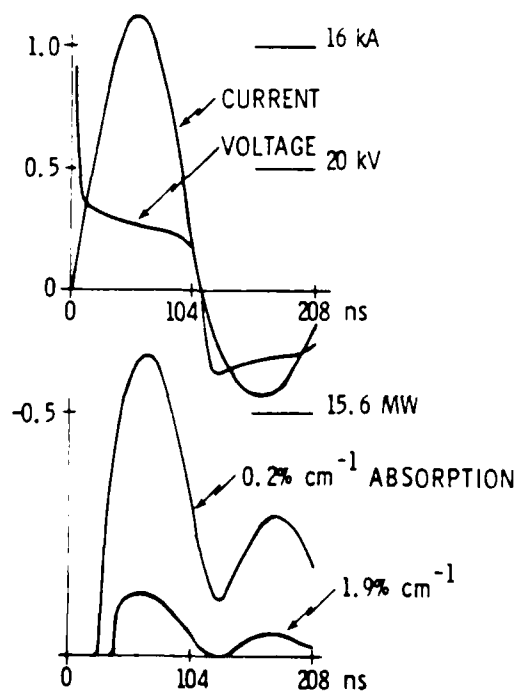


FIGURE 28. WAVEFORMS FOR ONE-STAGE PFN WITH KrF

The voltage rises to approximately equal the charging voltage and then drops quickly as the discharge breaks down. The fall time is governed by the ionization rate, which is a function of the electric field. The voltage flattens out as it approaches the static breakdown voltage and remains fairly constant until the current begins to swing around and pull everything through zero. At this point, if there is still charge on the capacitor, the process begins again. In Figure 28, the circuit is underdamped and there is enough power in the negative swing to exceed laser threshold a second time. In actual practice, the depletion of fluorine, the buildup of absorbers, and the onset of instabilities usually combine to prevent this occurrence.

The rise time of the current for a single-stage LC network is limited to a large fraction of the pulse length. Hence the loss due to spontaneous emission in the initial buildup phase may be excessive. In order to speed up the current rate of rise, a second stage in the form of a peaking capacitor may be added to the circuit as in Figure 29. Now the primary capacitor charges the peaking capacitor through  $L_1$  and then discharges into the gas through a much smaller  $L_2$ . The waveforms for this circuit are shown in Figure 30. Note that the current now rises much more steeply. However, the individual pulse widths are much shorter, as the peaking capacitor alternately charges and discharges through the load. This multiple pulsing can be alleviated by choosing a larger peaking capacitor to make the characteristic times of the two loops more comparable.

The increased current rise time achieved with a peaking capacitor does not come free. As one can see from Figure 30, the voltage rise time is now considerably slower due to the time required to charge  $C_2$ . A slow voltage rise can have a detrimental influence on discharge stability. The reason for this can be seen by looking at the dependence of ionization rate on electric field. Just above the breakdown potential, the net ionization rate is changing rapidly with applied field. The rate of change decreases as the field increases. With a slow voltage rise, the electric field spends a long time just above breakdown and any slight non-uniformities in the field can lead to large variations in electron density which may develop into arcs. The way to overcome this problem, of course, is to include a series peaking switch to hold the voltage off the discharge until  $C_2$  is fully charged. The drawback

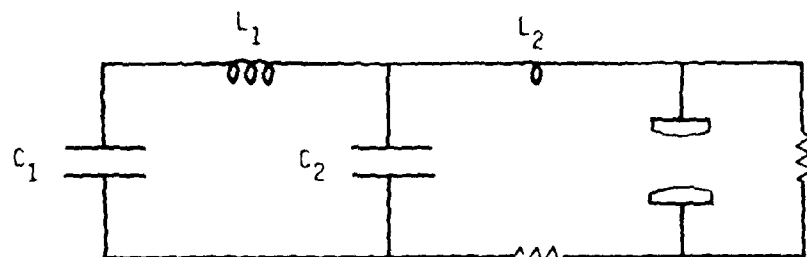


FIGURE 29. TWO-STAGE PFN

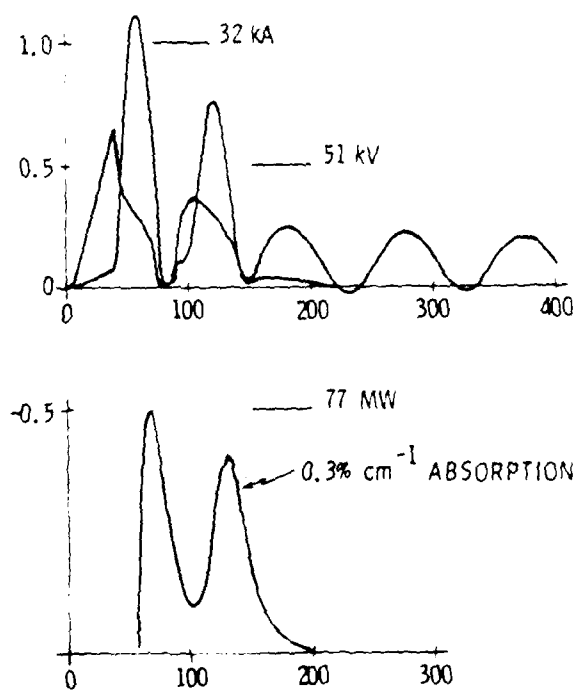


FIGURE 30. WAVEFORMS FOR TWO-STAGE PFN WITH KrF

to this is that it adds inductance to the secondary loop which again slows down the current rise. A low inductance multichannel rail gap may provide the ultimate solution, however, as we found experimentally, the improvement may not be dramatic.

The circuit used to describe the LTDD device is shown in Figure 31. The capacitor,  $C_M$ , represents either the fully-erected Marx generator or a peaking capacitor which is charged by the Marx. The capacitors,  $C_D$ , represent the capacitance between the imbedded electrodes and the gas, and  $C_G$  is the transverse capacitance of the gas. The variable resistors,  $R_T$  and  $R_L$ , are the transverse and longitudinal discharge impedances, respectively.

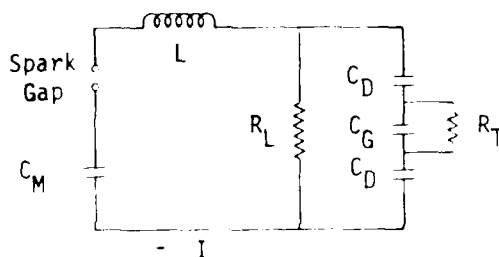


Figure 31. Circuit and Discharge Model

The discharge is assumed to take place uniformly within the volume so that total transverse and longitudinal currents are respectively,

$$I_T = J_T w l \quad \text{and} \quad I_L = J_L w d \quad (5.1)$$

where  $w$  and  $l$  are the discharge width and length, and  $d$  is the separation of dielectric surfaces. The discharge impedances are given by,

$$R_T = \frac{d}{w l} \frac{1}{\sigma} \quad \text{and} \quad R_L = \frac{l}{w d} \frac{1}{\sigma} \quad (5.2)$$

where  $\sigma$  is the plasma conductivity, which can be written in terms of the electron density and mobility as  $\sigma = e n_e \mu_e$ . The electron number density satisfies the continuity equation.

$$\frac{\partial n_e}{\partial t} = z n_e - \beta n_e - \gamma n_e^2 \quad (5.3)$$

The rates on the right side of Equation (5.3) are direct ionization,  $z$ , electron attachment,  $\beta$ , and recombination,  $\gamma$ . Two-step ionization via metastable states of the rare gas has been omitted in this case. The

coefficients  $z$ ,  $\epsilon$ , and  $\mu_e$  are functions of the total electric field in the plasma,  $E = \sqrt{E_T^2 + E_L^2}$ .

The waveforms generated by the TLDD model are shown in Figure 32 for two different charging voltages. The parameters used were

$$d = 25.4 \text{ cm}$$

$$w = 6.7 \text{ cm}$$

$$C_\mu = 675 \text{ pF}$$

$$C_D = 66 \text{ pF}$$

$$C_G = 7.5 \text{ pF}$$

$$L = 3.2 \text{ } \mu\text{H}$$

The quantity  $Q_M$  in Figure 32 is the charge remaining on capacitor,  $C_M$ . For both charging voltages considered, this capacitor is never fully discharged. The glow essentially goes out before the supply is fully drained. This problem is more severe at lower voltages. There is also some charge left on the dielectric, which rings back and forth between  $C_M$  and  $C_D$  causing an oscillation in the current at late times.

The current and voltage waveforms in Figure 32 are similar to those seen experimentally on the TLDD. The principal difference is in the voltage. The experimental voltage goes through two peaks and then oscillates around zero (Figure 16), while the model shows the voltage remaining positive. There are two likely explanations for the discrepancy. First, the model does not include two-step ionization which would cause the impedance to fall below that shown in Figure 32. Second, the experiment allows charge to flow out of the peaking capacitor back into the Marx generator, which would cause the voltage across the discharge to drop.

The power dissipated by the discharge is

$$P_d = \vec{J} \cdot \vec{E} = en_e \mu_e E^2 \quad (5.4)$$

This function fluctuates in time with a period of about 24 ns at the lower charging voltage and 18 ns at the higher. These periods do not correspond

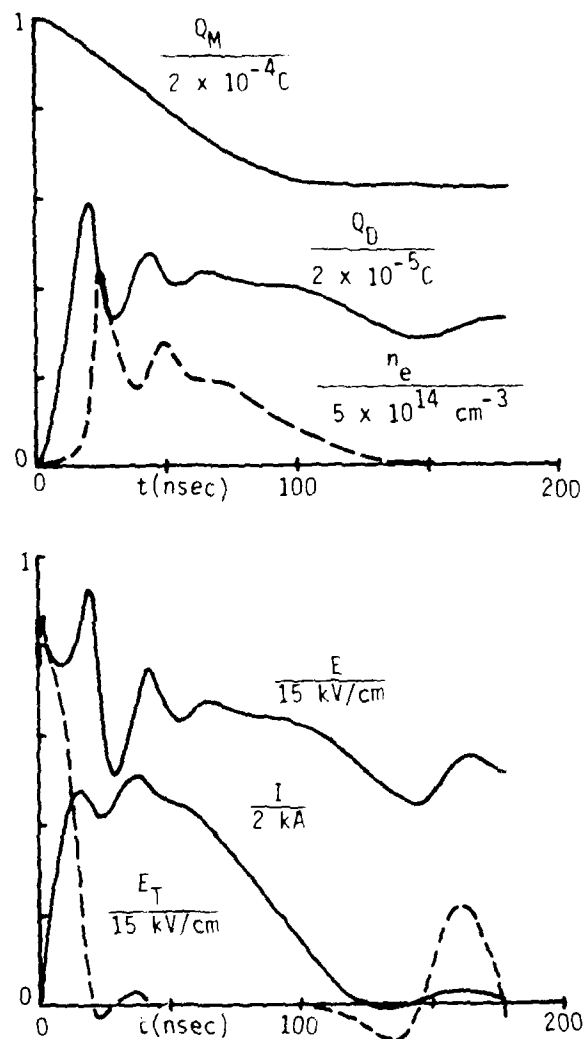


FIGURE 32(A). RESULTS OF MODEL CALCULATIONS ;  $V_0 = 300 \text{ kV}$



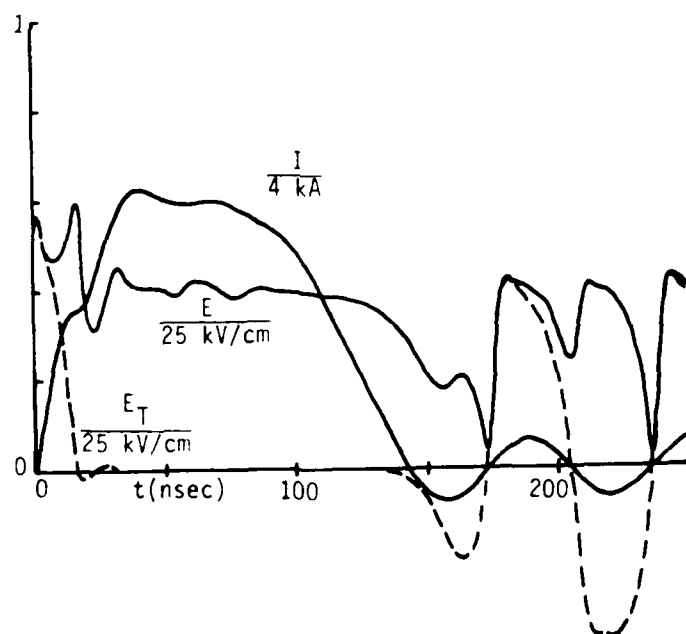
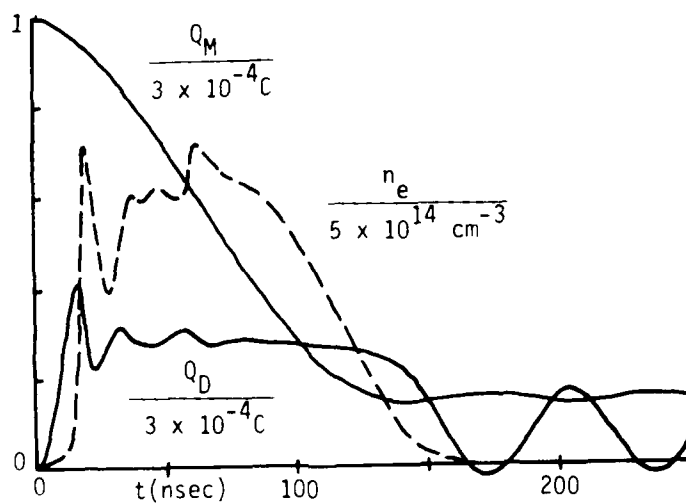


FIGURE 32(B). RESULTS OF MODEL CALCULATIONS;  $V_0 = 450 \text{ kV}$

with any  $\sqrt{LC}$  time for the circuit but are related to the kinetics of the breakdown mechanism itself. Notice that the transverse field is neutralized in a short time and that the power dissipated by the transverse discharge is very small. It therefore serves its purpose effectively as a preionizer. The oscillation in the transverse field late in time is too weak to reignite the discharge.

## 5.2 Discharge Kinetics

The discharge kinetics were modeled by a set of coupled continuity equations for the electron, negative halogen ion, rare-gas metastable, and upper laser level densities. This analysis couples self-consistently to the external circuit and laser cavity models through the discharge impedance and inversion density, respectively. The rate constants for collisions between heavy particles were taken from the literature, while those involving electrons were derived from the relevant cross section data by convolution with the electron energy distribution function,  $f_0(\epsilon)$ :

$$K\left(\frac{E}{N}\right) = \sqrt{\frac{2e}{m}} \int_0^\infty Q(\epsilon) f_0\left(\frac{E}{N}, \epsilon\right) \epsilon d\epsilon. \quad (5.5)$$

The electron energy distribution was determined by solving the collisional Boltzmann equation with the appropriate elastic and inelastic cross sections. The Boltzmann equation for a single component gas is given in integral form by

$$f_0(\epsilon) = \exp \left\{ - \frac{3}{(E/N)^2} \int_0^\epsilon \left( \frac{2m Q Q_m \epsilon'}{M} \right. \right. \quad (5.6)$$

$$\left. + \frac{Q}{\epsilon' f_0(\epsilon')} \sum_j \int_{\epsilon'}^{\epsilon' + \epsilon_j} \epsilon'' Q_j(\epsilon'') \left[ f_0(\epsilon'') - \frac{N_j}{N_0} f_0(\epsilon'' - \epsilon_j) \right] d\epsilon'' \right\} d\epsilon'$$

where the sum is taken over all inelastic processes,  $Q_j$ , with excited state densities  $N_j$  and energy losses  $\epsilon_j$ .

$$\begin{aligned}
N_0 &= \text{ground state density} \\
m &= \text{electron mass} \\
M &= \text{atomic mass} \\
Q_m &= \text{momentum transfer cross section} \\
Q &= Q_m + \sum_j Q_j
\end{aligned}$$

Additional summations are to be included for multiple component gas mixtures. Equation (5.6) is solved by iteration for  $f_0(\epsilon)$  which is normalized such that

$$\int_0^\infty f_0(\epsilon) \epsilon^{1/2} d\epsilon = 1. \quad (5.7)$$

The electron drift velocity,  $w\left(\frac{E}{N}\right)$ , is then given by

$$w\left(\frac{E}{N}\right) = \sqrt{\frac{2e}{m}} \int_0^\infty f_1(\epsilon) \epsilon d\epsilon \quad (5.8)$$

where

$$f_1(\epsilon) = -\frac{E/N}{Q} \frac{\partial f_0}{\partial \epsilon} \quad (5.9)$$

is the anisotropic part of the distribution function. The drift velocity is used in determining the discharge impedance,  $R$ , as follows: The current density is

$$J = enw\left(\frac{E}{N}\right) \quad (5.10)$$

where  $n$  is the electron number density (the contribution of the heavy ions to the current is negligible). Assuming a uniform electric field and charge distribution, the total current through the discharge with cross sectional area,  $A$ , is

$$I = eAnw\left(\frac{E}{N}\right) \quad (5.11)$$

and the discharge impedance with an electrode separation,  $d$ , is

$$R = \frac{Ed}{eAnw\left(\frac{E}{N}\right)} \quad (5.12)$$

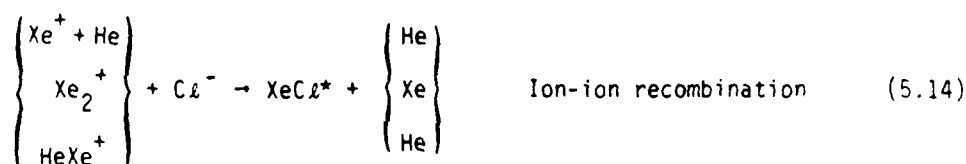
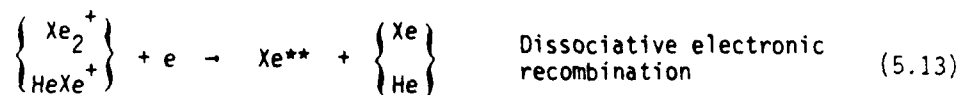
In modeling the XeCl laser, two gas mixtures were considered. A lean mix with 0.5 percent Xe and a rich mix with 2 percent Xe. The chlorine donor was HCl with a concentration of 1/30th of the Xe concentration in both cases. The balance of the gas was helium. The inelastic processes used in the Boltzmann calculation were

|       |   |                                |
|-------|---|--------------------------------|
| i)    | $\text{He}(1s, ^1S_0) \rightarrow \text{He}(2s, ^3S_1)$       | $\epsilon_j = 19.8 \text{ eV}$ |
| ii)   | $\text{He}(1s, ^1S_0) \rightarrow \text{He}(2p, ^3P_{0,1,2})$ | 20.9 eV                        |
| iii)  | $\text{He}(1s, ^1S_0) \rightarrow \text{He}(2p, ^1P_1)$       | 21.2 eV                        |
| iv)   | $\text{He}(1s, ^1S_0) \rightarrow \text{He}^+$                | 24.6 eV                        |
| v)    | $\text{He}(2s, ^3S_1) \rightarrow \text{He}^+$                | 4.8 eV                         |
| vi)   | $\text{Xe}(5s) \rightarrow \text{Xe}^*$                       | $\epsilon_j = 8.15 \text{ eV}$ |
| vii)  | $\text{Xe}(5s) \rightarrow \text{Xe}^+$                       | 12.13 eV                       |
| viii) | $\text{Xe}(6s) \rightarrow \text{Xe}^+$                       | 3.83 eV                        |
| ix)   | $\text{Xe}(6s) \rightarrow \text{Xe}(6p)$                     | 1.26 eV                        |
| x)    | $\text{Xe}(6s) \rightarrow \text{Xe}^{**}$                    | 2.24 eV                        |
| xi)   | $\text{HCl}(v=0) \rightarrow \text{HCl}(v=1)$                 | $\epsilon_j = 0.38 \text{ eV}$ |
| xii)  | $\text{HCl}(v=0) \rightarrow \text{HCl}(v=2)$                 | 0.68 eV                        |
| xiii) | $\text{HCl}(v=0) \rightarrow \text{H} + \text{Cl}^-$          | 0.74 eV                        |

The  $\text{Xe}^*$  state is a combined electronic state consisting of the 6s, 6p, and 5d configurations, while  $\text{Xe}^{**}$  comprises the remaining higher-lying states. All cross sections were taken from experimental data except for the excited-state excitation and ionization in xenon which were calculated using the classical formulation of Gryzinski.<sup>27</sup> Only collisions with the ground vibrational state of HCl were considered since the population in  $v=1$  is very small even at 600 K. The generation of  $v=1$  during the discharge was found to be negligible.

Selected rate constants for the lean mix are shown in Figures 33 and 34 as functions of E/N. Also shown is the electron mobility defined by  $\mu = W/E$ . In these calculations the number density of Xe(6s) states was taken to be 0.1 percent of the ground state xenon density. Discharge power partitioning into the various channels is shown in Figure 35. The optimum E/N for populating the Xe\* and Xe<sup>+</sup> states in this gas mixture is about 15 Td or 4 kV/cm-amagat. In the rich mix the optimum E/N is about 6 kV/cm-amagat.

Other reactions considered in the discharge kinetics model for XeCl were:



The branching ratios for the last two reactions into the XeCl(B) state were taken to be unity.

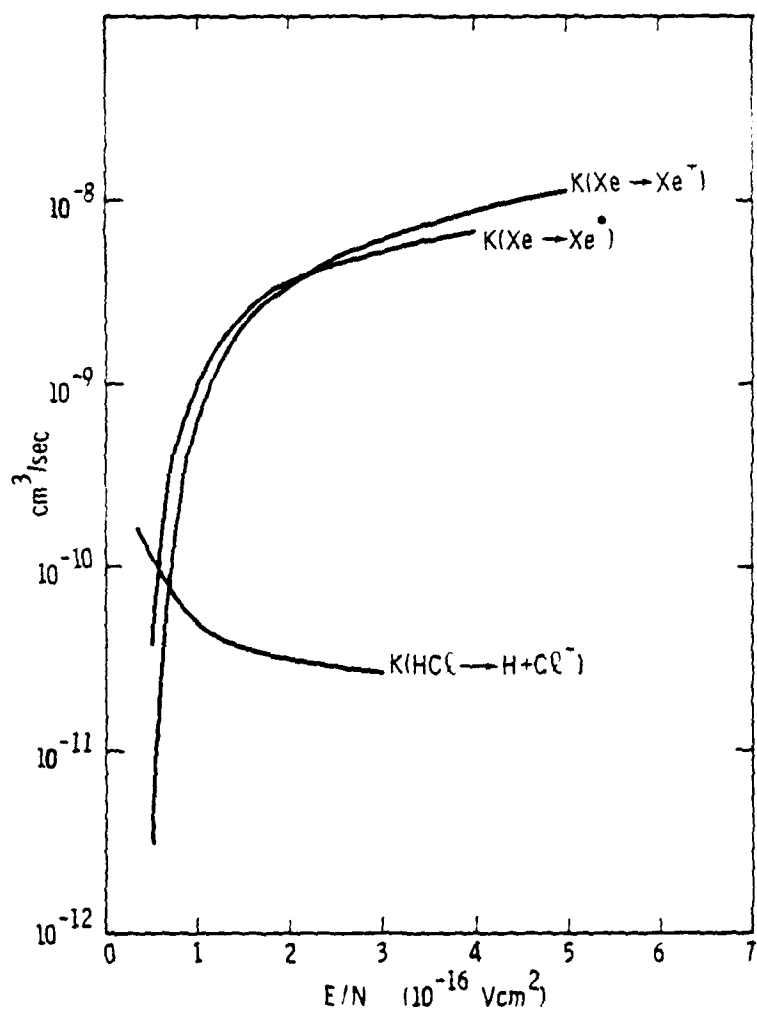


FIGURE 33. PRODUCTION AND LOSS OF ELECTRONS

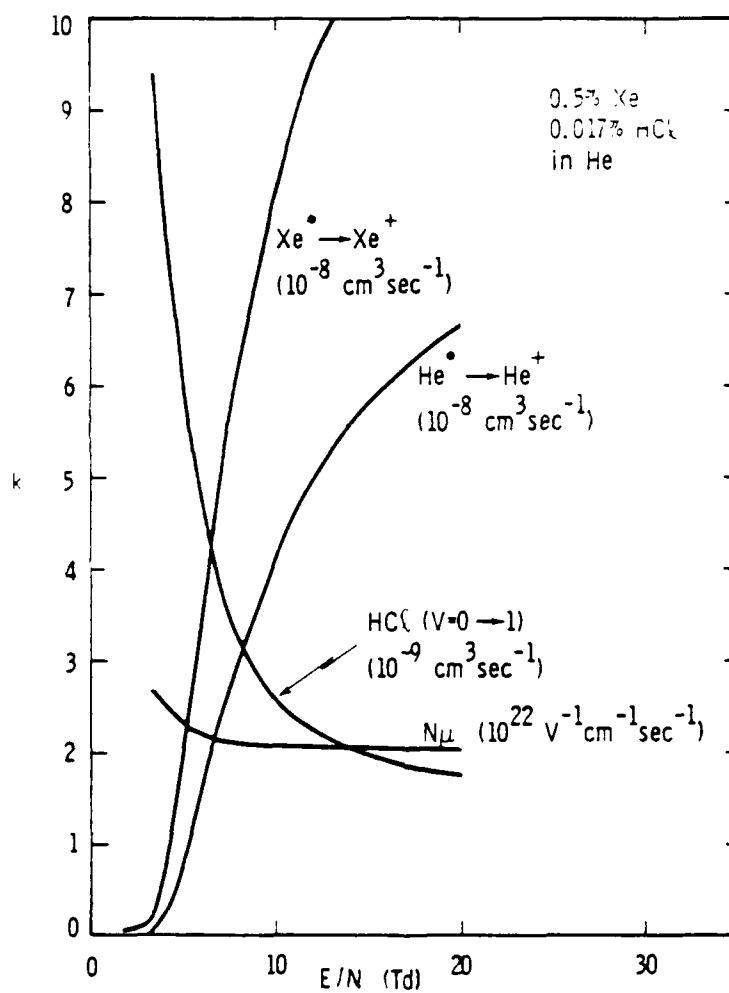


FIGURE 34. RATE CONSTANTS

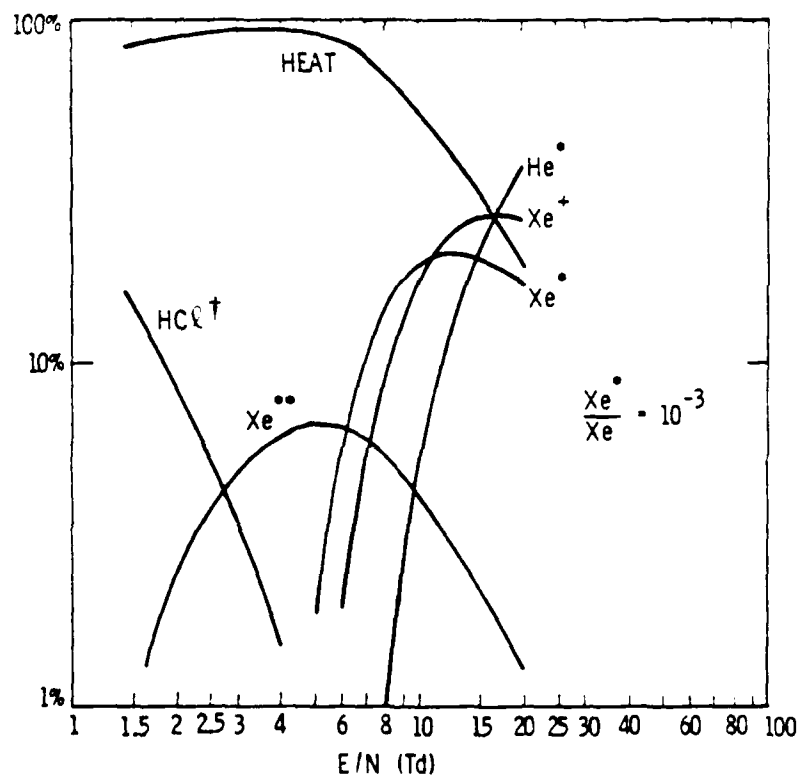


FIGURE 35. DISCHARGE POWER PARTITIONING  
IN 0.017% HC<sub>2</sub>, 0.5% Xe, 99.483% He



## 6.0 CONCLUSIONS

A unique transverse/longitudinal double-discharge-excited XeCl laser has been designed, built and tested with a number of electric pulse generating networks. Its experimentally determined electrical efficiency was 0.1 percent overall, or 0.5 percent based on energy deposited in the discharge volume prior and during the laser pulse. The theoretically predicted efficiencies between 2 and 3 percent could not be reached, because the longitudinal discharge showed arcing instabilities at xenon partial pressures above 10 Torr, thus preventing use of a kinetically favorable gas mixture. The instabilities manifested themselves in the form of surface-tracking arcs along the surfaces of the dielectric cavity walls.

Even with dilute mixtures of Xe and HCl in He, ionization instabilities in the discharge caused the electrode voltage to drop from above 200 kV to less than 50 kV during the pump pulse. This resulted in an average  $E/N$  of less than 7 Td. Calculations have shown (see Figure 35) that at such low  $E/N$  values close to 90 percent of the discharge energy goes into heating the gas and only approximately 10 percent into the production of  $\text{Xe}^*$  metastables and  $\text{Xe}^+$  ions, which are precursors to  $\text{XeCl}^*$  formation.

Further work aimed at improving the efficiency of longitudinal-discharge-excited high-pressure XeCl lasers will have to address and correct these two problem areas. These are:

1. Prevention of surface tracking in xenon-rich mixtures.
2. Improvement of the bulk discharge stability, to prevent rapid impedance collapse by two-step ionization runaway.

The surface tracking phenomenon is not well understood. It is definitely not an ordinary high-frequency skin effect. Simple calculations show that the skin depth for a typical discharge plasma is on the order of 10 cm for a 20 MHz pulse. Arguments can be brought forward, however, to support the notion that a sharp discontinuity in the dielectric constant (i.e., in the electrical permittivity) will promote surface tracking. For the present device this discontinuity at the surface of the dielectric was  $\epsilon_2/\epsilon_1 = 6/1$ .

Suggested follow-on experiments to the present work are:

1. The presence of dielectric surfaces in direct contact with the longitudinal discharge plasma may be avoided by adopting other methods of preionization, such as volume photoionization by a uv-laser beam.
2. If a "frustrated" transverse discharge is employed, a dielectric with a low  $\epsilon$  should be tried ( $\epsilon < 2.5$ ), and the dielectric surface should be set back from the longitudinal discharge volume.
3. A high-frequency ( $\sim 50$  MHz) transverse discharge may be used as a sustaining ionization source instead of as a simple preionizer. This may be particularly valuable in combination with a fast voltage rise-time ( $< 10$  ns) and a long rectangular pump pulse ( $> 100$  ns) for the main longitudinal discharge. Such a pump pulse may be generated<sup>2</sup> with a parallel-plate waterline, for example.

## 7.0 REFERENCES

1. D. E. Rothe, J. B. West and M. L. Bhaumik, "Efficient e-beam excitation of XeCl," IEEE J. Quant. Electron. QE-15, 314 (1979).
2. J. I. Levatter and S. C. Lin, "Necessary conditions for the homogeneous formation of pulsed avalanche discharges at high gas pressures," J. Appl. Phys. 51, 210 (1980).
3. W. L. Nighan and W. J. Wiegand, "Influence of negative-ion processes on steady-state properties and striations in molecular gas discharges," Phys. Rev. A10, 922 (1974).
4. H. Komine and E. A. Stappaerts, "Efficient Raman conversion of excimer lasers into the blue-green" ONR/NOSC Contract No. N00014-78-C-0032, Final Report (to be published); also "Frequency Conversion Techniques," Northrop IR&D Project No. 79-R-540.
5. E. J. Schimitschek and J. E. Celto, "Mercuric bromide dissociation laser in an electric discharge," Opt. Lett. 2, 64 (1978).
6. R. Burnham, "Discharge pumped mercuric halide dissociation lasers," Appl. Phys. Lett. 33, 156 (1978).
7. E. J. Schimitschek and J. E. Celto, "Oscillator and oscillator-amplifier experiments with an HgBr<sub>2</sub>/HgBr dissociation laser," Appl. Phys. Lett. 36, 176 (1980).
8. S. C. Lin and J. I. Levatter, "X-ray preionization for electric discharge lasers," Appl. Phys. Lett. 34, 505 (1979).
9. J. L. Miller, J. Dickie, J. Davin, J. Swingle and T. Kan, "Operating characteristics of a closed-cycle-flow rare-gas halide laser," Appl. Phys. Lett. 35, 912 (1979).
10. L. Burlamacchi, P. Burlamacchi and R. Salimbeni, "Long-life operation of an XeCl excimer laser," Appl. Phys. Lett. 34, 33 (1979).
11. H. Komine and E. A. Stappaerts, "Efficient higher-Stokes-order Raman conversion in molecular gases," Optics Lett. 4, 398 (1979).
12. R. Burnham and N. Djeu, "Efficient Raman conversion of XeCl-laser radiation in metallic vapors," Opt. Lett. 3, 215 (1978).

13. D. Cotter and W. Zapka, "Efficient Raman conversion of XeCl excimer laser radiation in Ba vapor," Opt. Commun. 26, 251 (1978).
14. D. E. Rothe and R. A. Gibson, "Analysis of a spark-preionized large-volume XeF and KrF discharge laser," Optics Commun. 22, 265 (September 1977).
15. D. E. Rothe and R. A. Gibson, "Parametric and scaling studies of self-sustained discharge-excited rare-gas halide lasers," Proceedings of Army Symposium on New Concepts in Lasers, U.S. Army MIRACOM special report H-77-3, Redstone Arsenal Alabama, (July 1977), p. 190.
16. D. E. Rothe, "Parametric and scaling studies of spark-preionized discharge-excited rare-gas halide lasers," Paper CA-7, 30th Annual Gaseous Electronics Conference, Palo Alto, California, (18-21 October 1977).
17. R. Butcher and W. L. Willis, "Measured discharge voltage and current characteristics of a cable-driven Tachisto-type KrF laser (0.6 m long electrodes separated by 1.9 cm)," Los Alamos Scientific Laboratory, Los Alamos, New Mexico (LASL Report, 1977), unpublished.
18. V. N. Ishchenko, V. N. Lisitsyn, and A. M. Razhev, "Efficient discharge pumping of XeCl laser," Opt. Commun. 21, 30 (1977).
19. P. Burnham, "Improved performance of the discharge-pumped XeCl laser," Opt. Commun. 24, 161 (1978).
20. P. C. Sze and F. B. Scott, "Intense laser action of XeCl, KrCl, and XeBr in large volume electric discharges," Los Alamos Scientific Laboratory work reported at 10th International Quantum Electronics Conference, Atlanta, Georgia, (29 May - 1 June 1978).
21. R. Burnham and G. Djeu, "Ultraviolet-preionized discharge pumped lasers in XeF, KrF and ArF," Appl. Phys. Lett. 29, 707 (1976).
22. W. J. Sarjeant, A. J. Alcock, and K. E. Leopold, "A scalable multi-atmosphere high-power XeF laser," Appl. Phys. Lett. 30, 635 (1977).

23. A. K. Laflamme, "Double discharge excitation for atmospheric pressure  $\text{CO}_2$  lasers," Rev. Sci. Instr. 41, 1578 (1970).
24. V. N. Ischenko, V. N. Lisitsyn, A. M. Razhev, V. N. Starinsky, and P. L. Chapovsky, "The  $\text{N}_2^+$  laser," Optics Commun. 13, 231 (1975).
25. D. E. Rothe, M. L. Bhaumik and W. H. Long, "Self-sustained visible and ultraviolet lasers", Northrop PTO Independent R&D Project Description 80-R-537 (1980).
26. F. M. Bruce, "Calibration of uniform-field spark-gaps for high-voltage measurement at power frequencies", J. IEEE Pt. II, 138 (1947).
27. M. Gryzinski, "Classical theory of atomic collisions. I. Theory of Inelastic Collisions", Phys. Rev. 138, A336 (1965).

END

DATE  
FILMED

12-81

DTIC